

Arecibo observations of a burst storm from FRB 20121102A in 2016

D. M. Hewitt,¹  M. P. Snelders,¹ J. W. T. Hessels,^{1,2} K. Nimmo,^{1,2} J. N. Jahns,³ L. G. Spitler,³ K. Gourdji,¹ G. H. Hilmarsson,³ D. Michilli,^{4,5} O. S. Ould-Boukattine,¹ P. Scholz,⁶ A. D. Seymour⁷

¹ Anton Pannekoek Institute for Astronomy, University of Amsterdam, Science Park 904, 1098 XH Amsterdam, The Netherlands

² ASTRON, Netherlands Institute for Radio Astronomy, Oude Hoogeveensedijk 4, 7991 PD Dwingeloo, The Netherlands

³ Max-Planck Institute for Radio Astronomy, Auf dem Hügel 69, D-53121 Bonn, Germany

⁴ MIT Kavli Institute for Astrophysics and Space Research, Massachusetts Institute of Technology, 77 Massachusetts Ave, Cambridge, MA 02139, USA

⁵ Department of Physics, Massachusetts Institute of Technology, 77 Massachusetts Ave, Cambridge, MA 02139, USA

⁶ Dunlap Institute for Astronomy & Astrophysics, University of Toronto, 50 St. George Street, Toronto, ON M5S 3H4, Canada

⁷ Green Bank Observatory, P.O. Box 2, WV 24944, Green Bank, USA

Accepted XXX. Received YYY; in original form ZZZ

ABSTRACT

FRB 20121102A is the first known fast radio burst (FRB) from which repeat bursts were detected, and one of the best-studied FRB sources in the literature. Here we report on the analysis of 478 bursts from FRB 20121102A using the 305-m Arecibo telescope, detected during approximately 59 hours of observations between December 2015 and October 2016. The majority of bursts are from a burst storm around September 2016. This is the earliest available sample of a large number of FRB 20121102A bursts, and it thus provides an anchor point for long-term studies of the source’s evolving properties. We observe that the bursts separate into two groups in the width-bandwidth-energy parameter space, which we refer to as the low-energy bursts (LEBs) and high-energy bursts (HEBs). We find that the LEBs are typically longer duration and narrower bandwidth than the HEBS. This is reminiscent of the spectro-temporal differences observed between the bursts of repeating and non-repeating FRBs. We fit the cumulative burst rate-energy distribution with a broken power-law and find that it flattens out toward higher energies. The bursts in this sample comprise a diverse zoo of burst morphologies, but notably burst emission seems to be more common at the top than the bottom of our observing frequency range ($\sim 1150 - 1730$ MHz). We also observe that bursts from the same day appear to be more similar to each other than to those of other days, but this observation requires confirmation. The wait times and burst rates that we measure are consistent with previous studies.

Key words: (transients:) fast radio bursts – methods: data analysis

1 INTRODUCTION

Fast radio bursts (FRBs) are flashes of radio emission with exceptionally high isotropic equivalent luminosity that usually last no longer than a few tens of milliseconds and originate at extragalactic distances (Lorimer et al. 2007; Thornton et al. 2013; Petroff et al. 2019, 2021; Cordes & Chatterjee 2019). Hundreds of FRBs have been detected to date (see the Transient Name Server¹ or Petroff et al. 2016; The CHIME/FRB Collaboration et al. 2021a), but only approximately 20 of these sources are known to repeat (e.g. Spitler et al. 2016; Shannon et al. 2018; Kumar et al. 2019; CHIME/FRB Collaboration et al. 2019a,b; Fonseca et al. 2020). Over a dozen FRBs (both repeating as well as apparently non-repeating) have been localised to a variety of host galaxies (Bhandari et al. 2021), but the emission mechanism and physical origin remain enigmatic. While the repeaters rule out cataclysmic models for at least some fraction of the FRB population, the models that have been proposed for FRBs span a wide range of astrophysical scenarios (for a catalogue of models see Platts

et al. 2019). In recent years, there has been a noteworthy detection of an extremely bright radio burst from the Galactic magnetar SGR J1935+2154 (Bochenek et al. 2020; CHIME/FRB Collaboration et al. 2020) which has strengthened the case for magnetars as the engines of FRBs. Even so, the discovery of a nearby repeating FRB in a globular cluster shows that not all FRBs can be young magnetars formed via core collapse (Kirsten et al. 2021) — though they may be, in some cases, young magnetars formed via accretion-induced collapse or binary merger.

It remains unclear whether the repeating and apparently non-repeating FRBs come from physically distinct source types. Recently, it has been shown that the burst properties of repeating and non-repeating FRBs are statistically different, with repeaters on average exhibiting larger temporal widths and narrower bandwidths (Pleunis et al. 2021; The CHIME/FRB Collaboration et al. 2021a). Additionally, many repeater bursts display complex time-frequency downward-drifting structure (the ‘sad-trombone’ effect; Hessels et al. 2019). Another commonality that seems to be emerging among repeating sources, is near 100 per cent linear polarisation, a very low circular polarisation fraction and polarisation position angles (PPAs) that remain approximately constant between and dur-

* E-mail: d.m.hewitt@uva.nl

¹ <https://www.wis-tns.org>

ing bursts (Michilli et al. 2018b; Nimmo et al. 2021b). While there have been a small number of detections of circular polarisation in repeater bursts (Hilmarsson et al. 2021a; Kumar et al. 2021) and swinging PPAs (Luo et al. 2020), the non-repeating FRB population shows more diverse polarimetric properties (e.g. Day et al. 2020). These differences in the burst properties of repeaters and apparent non-repeaters could indicate different emission mechanisms, different progenitors and/or different local environments.

FRB 20121102A is the first FRB source from which multiple bursts were detected (Spitler et al. 2014, 2016). This repeating nature allowed for follow-up observations that localised the source to near a star-forming region in a dwarf galaxy at redshift $z = 0.193$ (Bassa et al. 2017; Chatterjee et al. 2017; Tendulkar et al. 2017) and, moreover, a milliarcsecond association of the bursts with a persistent compact radio source (Marcote et al. 2017). The most recent dispersion measure (DM) measurements of the bursts from FRB 20121102A are $563.5 \pm 0.8 \text{ pc cm}^{-3}$ on MJD 57836 (Platts et al. 2021) and $565.8 \pm 0.8 \text{ pc cm}^{-3}$ for the period between MJD 58724 and MJD 58776 (Li et al. 2021). Li et al. (2021) also estimated that this DM is increasing by approximately $1 \text{ pc cm}^{-3} \text{ yr}^{-1}$. Moreover, there is evidence that this secular DM increase is non-linear (Jahns et al. *in prep.*, Seymour et al. *in prep.*). Michilli et al. (2018b) showed that FRB 20121102A has an extremely large and variable rotation measure ($\text{RM} \sim 10^5 \text{ rad m}^{-2}$), demonstrating that the bursts originate from a source embedded in an extreme and dynamic magneto-ionic environment. In contrast to the DM, the RM of the bursts is decreasing by an average of ~ 15 per cent year^{-1} (Hilmarsson et al. 2021b). The bursts from FRB 20121102A show all the properties typically associated with repeating FRBs mentioned previously, but the burst profile and spectrum can change significantly from burst to burst. It is also worth mentioning that the burst activity of FRB 20121102A appears to be frequency dependent. While thousands of bursts were detected in less than two months in the 1–2 GHz range (L-band) (Li et al. 2021), only one burst has been detected in the 400–800 MHz range (more specifically ~ 600 MHz; Josephy et al. 2019) despite years of nearly daily monitoring by the Canadian Hydrogen Intensity Mapping Experiment Fast Radio Burst Project (CHIME/FRB). On the other extreme, the highest frequency at which bursts have been detected from FRB 20121102A (and from any FRB for that matter) is ~ 8 GHz (Gajjar et al. 2018). From a temporal point of view, the bursts from FRB 20121102A are clustered in time (Oppermann et al. 2018), but show no evidence of a rotational period underlying their times-of-arrival (Zhang et al. 2018; Aggarwal et al. 2021). Analysis of burst data over 5 years has, however, resulted in an activity period of ~ 160 days and a duty cycle of ~ 55 per cent (Rajwade et al. 2020; Cruces et al. 2021). FRB 20121102A is one of only two known FRB sources with a long-term periodicity: the other being FRB 20180916B, which has a well-established activity period of 16.35 days with an activity window of ~ 5 days. (Chime/Frb Collaboration et al. 2020).

Various models have been proposed to explain the repeating nature and periodic activity of some FRBs, typically by either invoking precession of a neutron star (NS) (e.g. Levin et al. 2020; Sob'yanin 2020; Yang & Zou 2020; Zanazzi & Lai 2020), the rotational period of a NS (e.g. Beniamini et al. 2020, although *such* slow-rotating magnetars have not yet been observed) or the orbital period of a NS in a binary system with another astrophysical object (e.g. Gu et al. 2020; Lyutikov et al. 2020; Du et al. 2021; Kuerban et al. 2021; Wada et al. 2021). The literature is also divided on the location of the emission region, assuming a NS origin: either within the magnetosphere of the NS (e.g. Kumar et al. 2017), or much further out beyond the

magnetosphere as the result of relativistic shocks (e.g. Metzger et al. 2019).

The spectro-temporal and polarimetric properties of the bursts, as well as their energetics and the evolution of these factors, are all valuable probes for constraining and differentiating between progenitor models. The short time intervals between bursts and high burst rate of bursts detected by FAST (Five hundred meter Aperture Spherical Telescope) favour those models where burst genesis occurs in the magnetosphere (Li et al. 2021). Burst structure down to $\sim 4 \mu\text{s}$ and $\sim 60 \text{ ns}$ is detected in FRB 20180916B and FRB 20200120E, respectively (Nimmo et al. 2021a,b). This also supports magnetospheric models since, ignoring relativistic effects, these durations correspond to an emission region from $\sim 100 \text{ m}$ to a few km in size. The sad-trombone effect can be explained as a radius-to-frequency mapping effect in magnetospheric models (Lyutikov 2020), but is also a natural consequence of models invoking synchrotron maser models (e.g. Metzger et al. 2019; Margalit et al. 2020).

Through a monitoring proposal (P3054; PI: L. Spitler) the Arecibo Observatory's 305-m telescope has been used to detect over a thousand bursts from FRB 20121102A since its discovery. In this paper we present analysis of the earliest observed burst storm of FRB 20121102A. In §2, we describe the observations and our search analysis used to discover the bursts presented in this work. In §3 we present the search results and explain how the burst properties have been measured. We describe how we classify bursts as either 'low-energy bursts' or 'high-energy bursts', and evaluate the statistical significance of this classification. We also explain our procedures of fitting power-laws to the energy distribution of the detected bursts. In §4 we investigate how the classification of low- and high-energy bursts relates to what is known from other FRBs. Furthermore, we discuss the results of the energy and spectro-temporal properties of this sample of bursts. Finally, in §5 we summarise our main findings.

2 OBSERVATIONS AND SEARCH FOR BURSTS

We observed FRB 20121102A with the 305-m William E. Gordon Telescope at the Arecibo Observatory using the L-wide receiver. In this paper, we report on 56 observations that sum to ~ 59 hours on source. These observations were conducted on different days, sometimes consecutive, between November 2015 and October 2016, and are summarised in Table 1. The data were recorded using the Puerto-Rican Ultimate Pulsar Processing Instrument (PUPPI) backend recorder², which records from 980–1780 MHz and provides a time resolution of $10.24 \mu\text{s}$ and 512 frequency channels of width 1.56 MHz. The L-wide receiver has a smaller observing frequency range of 1150–1730 MHz, and the data outside this frequency range are excluded from analysis. These data were coherently dedispersed *within* a channel to a DM of 557.0 pc cm^{-3} , the best DM measurement at the time of the observations, which effectively reduces intra-channel dispersive smearing to $< 30 \mu\text{s}$ given a true DM of 560.5 pc cm^{-3} (Hessels et al. 2019).

Prior to searching for bursts, we downsampled the data using `psrfits_subband`³, resulting in 64 channels of 12.5 MHz and a time resolution of $81.92 \mu\text{s}$. Using PRESTO⁴ (Ransom 2001), the data were searched for bursts by first incoherently dedispersing the time series using `prepsubband`, for 77 equally spaced trial DMs in the range 554.90 – $570.10 \text{ pc cm}^{-3}$ (steps of 0.2 pc cm^{-3}). No radio

² <http://www.naic.edu/puppi-observing/>

³ https://github.com/demorest/psrfits_utils

⁴ <https://www.cv.nrao.edu/~sransom/presto/>

frequency interference (RFI) masks were applied, in order to prevent masking very bright bursts. After this, the de-dedispersed time series' were searched with `single_pulse_search.py`, which implements matched boxcar filtering. Our search was most sensitive to bursts with boxcar widths between $81.92\ \mu\text{s}$ and $24.576\ \text{ms}$. We searched down to a S/N of 6 as provided by `single_pulse_search.py`. The detected pulses were grouped into burst candidates using SpS⁵ (Michilli et al. 2018a). Events within $20\ \text{ms}$ and $1\ \text{pc cm}^{-3}$ are grouped together.

The candidates were then classified with FETCH⁶ (Fast Extragalactic Transient Candidate Hunter; Agarwal et al. 2020), a supervised deep-learning algorithm that uses deep neural networks to classify burst candidates. FETCH has been trained on simulated FRBs and real RFI from the Green Bank Observatory's (GBT) L-band data (comparable frequencies to the Arecibo data presented in this paper). There are eleven models that all perform well on GBT data, and have also proven very successful at detecting FRBs with $\text{S/N} > 10$ in ASKAP (Australian Square Kilometre Array Pathfinder) and Parkes data. Since the Arecibo Observatory has additional disparate sources of RFI, and we also probe to a lower S/N than the training data, we first evaluated the performance of the different models through manual inspection using previously searched datasets which contained 41 known bursts (Gourdji et al. 2019). We found that model H performed the best at identifying true bursts. We managed to recover all bursts except for B33 from Gourdji et al. (2019). All diagnostic plots of candidates to which model H assigned a probability $p \geq 0.5$ had to undergo two independent by-eye inspections to be deemed true astrophysical bursts.

Two out of our 56 datasets have previously been analysed by both Gourdji et al. (2019) and Aggarwal et al. (2021). Aggarwal et al. (2021) also miss B33 from Gourdji et al. (2019), and speculate that it may be due the narrow-bandedness and low S/N of the burst. Additionally, Hessels et al. (2019) have reported on 14 bright bursts that are also included in our analysis here. We emphasise that even despite the large number of bursts found, there are possibly still bursts being missed due to the range of our boxcar widths used in searching, S/N-limitations and the model predictions of FETCH. Our sensitivity to bursts some factor shorter or longer than our minimum and maximum boxcar lengths decreases as a function of the square root of said factor. Furthermore, we do not implement any subbanded searches, which means we are less sensitive to very narrowband bursts from FRB 20121102A (bursts that extend over less than approximately a third of the observing bandwidth).

3 RESULTS AND ANALYSIS

A total of 478 bursts were determined to be of astrophysical origin in these observations, the majority of which were low S/N (see Figure A1). Due to the grouping of pulses within $20\ \text{ms}$ into burst candidates, there were a small number of instances (~ 7 per cent) where other nearby, much fainter bursts were also visible in addition to those pulses classified by FETCH. These bursts have been included in the total number of 478. Distinguishing between bursts and subbursts is also often non-trivial and becomes ambiguous at a certain level. In order to do so, we thus implemented the following definition: if a distinct Gaussian-like component in the frequency-averaged burst profile does not smear into other components but instead begins and ends at a baseline comparable to the noise, it is defined as a burst,

unless the component exists as one of the downward-drifting components often seen from repeaters (the sad-trombone effect), in which case we define it as a sub-burst. Figure 1 shows dynamic spectra of a sample of bursts that we detected and are either bright, very narrow or narrowband, or have complex frequency or time structure.

All bursts were dedispersed to a DM of $560.5\ \text{pc cm}^{-3}$, determined by Hessels et al. (2019), which maximised the band-integrated structure of the bursts and provided a smaller range (more than an order of magnitude) in the inferred DMs of the bursts than the DM which optimises S/N. When using `PsrfitsFile.read_subint`, the scales, weights and offsets need to be explicitly applied to prevent saturation of the brighter bursts as a result of previous downsampling. Given that the Arecibo observations in Hessels et al. (2019) are a sub-sample of the observations presented here, we choose this DM and assume that any change in the DM over the course of our observations is negligible. For each burst dynamic spectrum, the channels in which RFI were present were flagged and excluded from further processing. The dynamic spectra were then corrected for bandpass variations by subtracting the off-burst mean and dividing by the off-burst standard deviation, per channel. In Figure 1, in addition to dynamic spectra, we also show a time averaged spectrum, a full-band averaged burst time profile and the burst time profile obtained by only averaging over the frequencies where the burst is present (the 2σ region of a one-dimensional Gaussian fit to the burst spectrum). A one-dimensional Gaussian function is also fit to each full-band burst profile. The burst spectra are produced by time-averaging the dynamic spectrum over the 2σ region of this Gaussian fit. The 2σ regions of both Gaussian fits are indicated by green (and blue) shaded regions. We define the temporal width of a burst as the FWHM of the band-limited burst profile, and bandwidth as the 2σ region of the fit to the spectrum. We calculated the fluence of a burst by summing over the 2σ time region of a burst and then multiplying each channel of the spectrum with a channel-specific scaling based on the radiometer equation. Thereafter, the mean of the on-pulse spectrum is multiplied with the sampling time. This is equivalent to taking the product of the sampling time, the normalised time-profile and the radiometer equation.

$$F = \sum S/N \frac{\text{SEFD}(\nu, \theta_z)}{\sqrt{N_p \nu_{\text{ch}} t_{\text{samp}}}} \times t_{\text{samp}} \quad (1)$$

where S/N is the signal-to-noise ratio per channel, $\text{SEFD}(\nu, \theta_z)$ is the system equivalent flux density of Arecibo, which is dependent on the observing frequency (ν) and the zenith angle (θ_z), N_p is the number of polarisations (2 for the Arecibo L-wide receiver), ν_{ch} is the bandwidth of a single channel and t_{samp} the sampling time. In the literature, the gain (G) and system temperature (T_{sys}) of Arecibo have typically been approximated as $10.5\ \text{KJy}^{-1}$ and $30\ \text{K}$, respectively. We have modelled the SEFD ($= T_{\text{sys}}/G$) as a function of observing frequency and zenith angle, by fitting an exponential function to system performance measurements taken with the L-band wide receiver over a few years⁷. The sensitivity decreases as zenith angle increases and frequency decreases. This approach improves upon the standard convention of using one average value, as an SEFD $\approx 2.9\ \text{Jy}$ (often used in literature) can underestimate the SEFD by $\lesssim 25$ per cent on average.

⁵ <https://github.com/danielemichilli/SpS>

⁶ <https://github.com/devanshkv/fetch>

⁷ <http://www.naic.edu/%7Ephil/sysperf/sysperfbymon.html>

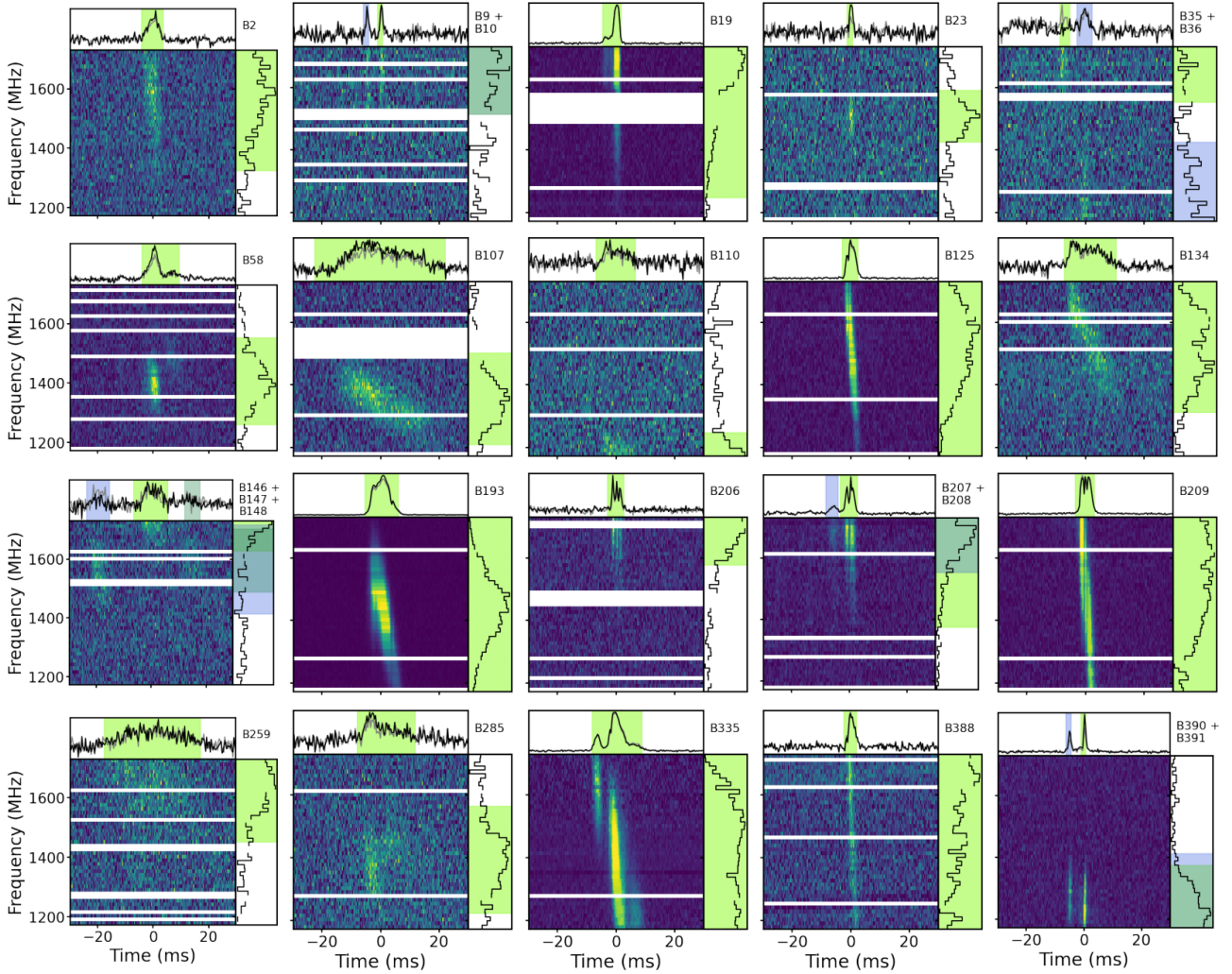


Figure 1. Dynamic spectra of a sample of the 478 detected bursts from FRB 20121102A. This sample contains bursts that are extremely bright, exhibit complex morphology or inhabit the extremes of the observing frequency range. Table A1 lists all 478 bursts and their properties. All bursts have been dedispersed to a DM of 560.5 pc cm^{-3} . The horizontal white stripes are channels that have been excised in order to remove radio frequency interference. The top panel of each thumbnail shows two burst profiles: one from summing over the entire observing band (in grey) and a second from only summing over the spectral extent where the burst is detected (in black). The panels on the right show the on-pulse time-averaged spectra. The green shaded areas indicate the 2σ region of Gaussian fits to the burst profile and spectrum. In the case where multiple bursts are present within a few tens of milliseconds, blue and darker green shaded areas indicate the 2σ region for these additional bursts. The burst number is displayed in the top right of each thumbnail. The dynamic spectra have been downsampled to a time and frequency resolution of $327.68 \mu\text{s}$ and 12.5 MHz , respectively. For visual purposes, the dynamic range of the colour scale is adjusted to saturate below the fifth percentile and above 95 per cent of the peak signal. Frequency and time axes are scaled equally to highlight the diversity in burst morphology. Three of the bursts displayed above, were also presented in [Hessels et al. \(2019\)](#) at higher time resolution with AO names: B125 (AO-02), B193 (AO-05), B209 (AO-06).

Finally, the isotropic equivalent burst energy⁸, E , is calculated as follows

$$E = \frac{4\pi F \Delta\nu D_L^2}{1+z} \quad (2)$$

where z is the redshift, F is the fluence of the burst (calculated only over the time- and frequency-extent of the burst), $\Delta\nu$ is the bandwidth

⁸ Even though the emission is expected to be beamed, we default to the isotropic equivalent energy because the beaming fraction is unknown.

of the burst and D_L is the luminosity distance to the host galaxy of FRB 20121102A (972 Mpc; [Tendulkar et al. 2017](#)).

The fluence of a burst can be calculated either over the entire observing frequency range (often the central observing frequency is used to offset the effect of varying instrumental bandwidths) or only over the extent of the burst. Common practice (e.g. [Law et al. 2017](#)) and recent recommendation (e.g. [Aggarwal 2021](#)) has preferred the latter. Importantly, however, when the isotropic equivalent energy is computed, one needs to consider the same regime as for the fluence estimation. Inconsistency in this matter may result in certain features of the burst energy distribution being diminished or accentuated.

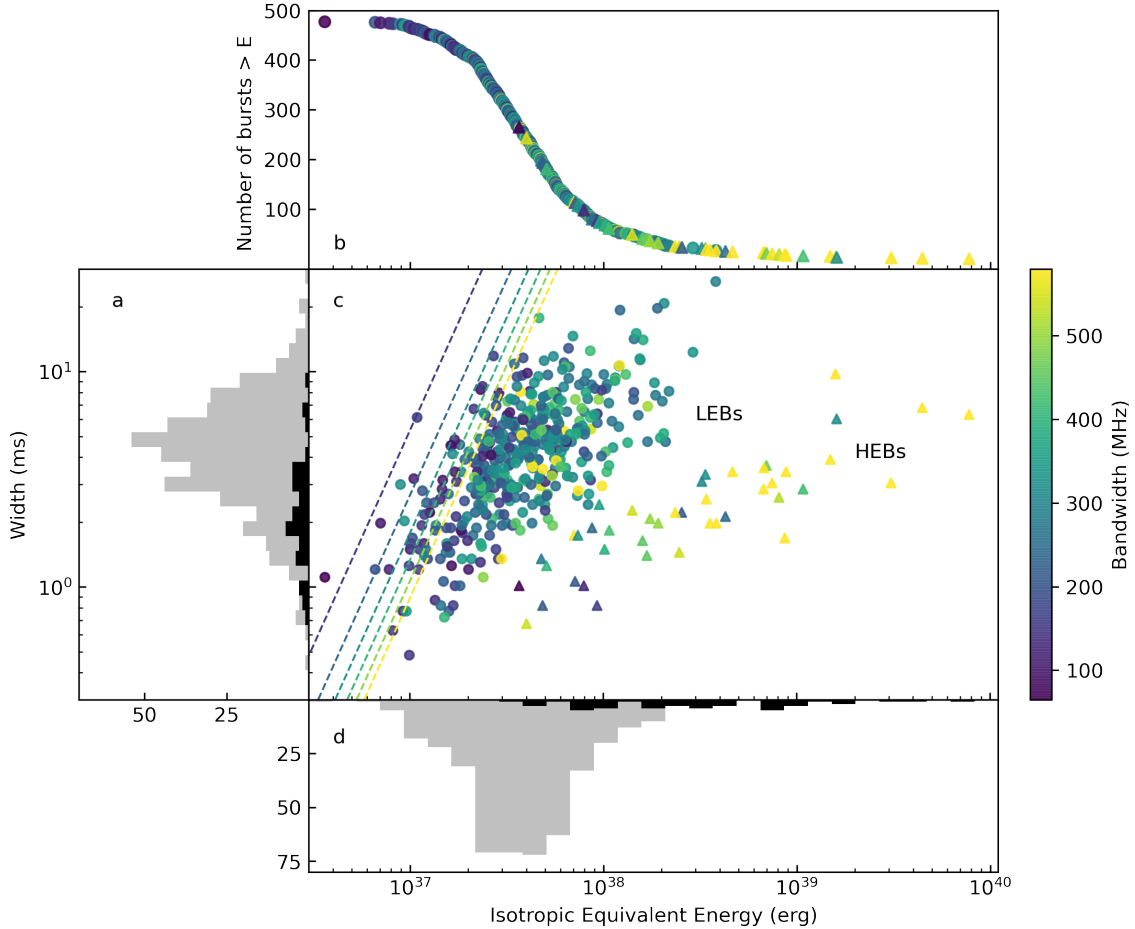


Figure 2. The 478 bursts have been clustered into two groups based on their width and energy as defined in §3.1, and these two clusters are depicted here as circles (the low-energy bursts or LEBs) and triangles (the high-energy bursts or HEBs). **a:** The width (FWHM) distributions of the bursts. The grey and black histograms correspond to the bursts indicated by circles (LEBs) and triangles (HEBs), respectively. **b:** The cumulative burst number-energy distribution. The data points are coloured according to the observed bandwidth of the bursts and correspond to the data points shown in Panel c. **c:** The burst width plotted against the isotropic equivalent energy for all bursts. The detection thresholds for bursts with a S/N of 6 and various bandwidths (multiples of 100 MHz) are indicated by slanted dashed lines which are also coloured according to observed bandwidth using the same scale as for the data points. **d:** Same as Panel a, but for isotropic equivalent burst energy rather than temporal width.

3.1 Grouping bursts and comparing groups

In Figure 2 the burst widths have been plotted against their isotropic equivalent energy, while also being coloured according to their observed bandwidth within the 1150–1730 MHz range we recorded. Our sample of bursts splits into two distinct groups in this three dimensional parameter space. We refer to these two groups as the low-energy bursts (LEBs) and high-energy bursts (HEBs). We employed a Gaussian Mixture Models (GMM) clustering algorithm using the `GaussianMixture.fit` method in the `sklearn.mixture` package⁹ (Pedregosa et al. 2011) to determine which bursts belong to which group. GMM clustering algorithms assume that all data points are from a combination of a finite number of Gaussian distributions – this is not necessarily true for our data, but we only use this clustering method as a quantitative means of classifying bursts as LEBs or HEBs. We disregard bandwidth and only take into account the temporal width and isotropic equivalent energy parameters (both in logarithmic space) for the clustering. We did so, firstly, because

the burst divide is most obvious in the width-energy plane. Secondly, the bandwidth is constrained by the maximum observing frequency range. While the bursts in our sample are also restricted to a range of temporal widths (due to boxcar lengths being searched) and energies (due to sensitivity limitations), the bandwidth is the only parameter where an abrupt cut-off is visible in its distribution. In Figure 2 the LEBs and HEBs have been plotted as circles and triangles, respectively. A total of 435 bursts were classified as LEBs and 43 as HEBs. Note that the LEBs typically have lower bandwidths than HEBs, and also larger temporal widths.

To determine whether the LEBs and HEBs can be drawn from the same parent population, we applied Kolmogorov-Smirnov (KS), Anderson-Darling (AD) and Epps-Singleton (ES) tests using the `ks_2samp`, `anderson_ksamp` and `epps_singleton_2samp` methods from the `scipy.stats` package¹⁰. The critical value for the KS test is approximately $D = c(\alpha) \sqrt{\frac{n_1+n_2}{n_1 n_2}} \approx 0.26$ where $c(\alpha) = 1.63$ is a coefficient corresponding to a significance level (α) of 0.01

⁹ <https://scikit-learn.org/stable/>

¹⁰ <https://docs.scipy.org/doc/scipy/reference/stats.html>

and $n_1 = 435$ and $n_2 = 43$ are the numbers of bursts classified as LEBs and HEBs, respectively. A KS-statistic larger than this value, or, equivalently, a small p-value (<0.001) can be used to reject the hypothesis that the samples are drawn from the same parent population. For the ES-test we followed the recommendation of Epps & Singleton (1986) and set the values where the empirical characteristic function will be evaluated to $t = (0.4, 0.8)$. The results of all these statistical tests are tabulated in Table 2. All three tests concur that we can reject the hypothesis that the bandwidth, width and fluence distributions between the two groups can be drawn from the same parent population.

To ensure that the statistically significant dissimilarity we see between the LEBs and HEBs is not merely the effect of a few outliers, we made use of a quasi-bootstrapping resampling method, whereby we ran 1000 trials, randomly resampling 10 per cent of the bursts from both the LEBs and HEBs by drawing from the LEB en HEB distributions, respectively (with replacement). For each trial of each parameter (width, bandwidth and fluence) we calculated the KS, AD and ES statistic and accompanying p-value. The mean p-values of this investigation are also in Table 2, and confirm that the statistical significance of our results is not dominated by a small number of outliers.

3.2 Burst energetics

In order to estimate the completeness limit of our observations, we assume a burst with a S/N of 6 that has a temporal width of 4.00 ms and a bandwidth of 275 MHz. These are the median values for width and bandwidth for all the bursts in our sample. Making use of Equations 1 and 2, we can then estimate the fluence or energy threshold below which our burst sample is incomplete. This limit is ~ 0.057 Jy ms, or $\sim 1.5 \times 10^{37}$ erg.

The cumulative energy distribution is usually approximated as a power-law $R(> E) \propto E^\gamma$, where R is the burst rate for bursts above some energy E and γ is the slope of the power-law. Fitting for a single power-law has proven to likely be an oversimplification when considering data over many orders of magnitude (Cruces et al. 2021). Moreover, Aggarwal (2021) have shown that the narrow-bandedness of bursts can greatly affect the shape of the observed energy distribution. Because many bursts are cut-off at the top or bottom of the observing window, energy distributions typically do not represent the energy distribution of bursts but rather of the emission within the observing frequency range. One can estimate the missing flux by assuming the spectral shape of the burst (which vary a lot between bursts) or by only selecting the bursts that appear to be fully within the observing window. This, however, also introduces a bias as the brightest broadband bursts will then be excluded. Approximating the energy distribution using slightly more complicated functions, for instance a broken power-law (Aggarwal et al. 2021) or a combination of a log-normal and Lorentz function (Li et al. 2021) have yielded better results. As has been discussed in Gourdji et al. (2019), correctly estimating the completeness threshold will also affect the interpretation of the results.

The rate-energy distribution of our sample of bursts can be seen in Figure 2b and Figure 3. We used `scipy.optimize.curve_fit`¹¹ to fit various power-laws to the energy distribution of our sample of bursts and subsets thereof. We excluded bursts that are below our calculated energy sensitivity threshold (i.e. $E_{\text{iso}} < 1.5 \times 10^{37}$ erg),

which make up ~ 8 per cent of the total sample. This threshold is indicated by a red vertical line in Figure 3 and the turn-over at low energies due to our sensitivity loss is also apparent here. The best fit was that of a double broken power-law to all the bursts above the sensitivity threshold. This fit yielded break energies of $E_{\text{b1}} = 3.1 \times 10^{37}$ and $E_{\text{b2}} = 2.3 \times 10^{38}$, with power-law slopes of -0.5 where $E_{\text{iso}} \leq E_{\text{b1}}$, -1.3 where $E_{\text{b1}} < E_{\text{iso}} < E_{\text{b2}}$, and -0.9 where $E_{\text{iso}} \geq E_{\text{b2}}$. We then repeated the process, only selecting the bursts above our sensitivity threshold that are mostly within the band (the 2σ region of the Gaussian fit to the spectrum is within the observing range of 1150 – 1730 MHz) or have a bandwidth larger than 500 MHz. This is done in an attempt to only account for those bursts for which we measure a significant fraction of the fluence. The results of this fit, those of other variants of power-laws, and to the LEBs and HEBs separately are presented in Table A2. We furthermore attempted to estimate the power-law index using the maximum likelihood method for different completeness thresholds, as described by Crawford et al. (1970) and James et al. (2019), but the power-law index does not converge towards a single value (see the right panel of Figure 3).

4 DISCUSSION

4.1 Low- and high-energy bursts

The classification of the bursts into two groups (LEBs and HEBs), as discussed in § 3.1, also appears to be consistent with what we can infer from the shape of the burst energy distribution. One of the breaks in the double power-law fit occurs at approximately the same energy where we find the transition between LEBs and HEBs (see Figure 3). Li et al. (2021) have reported that the energy distribution of FRB 20121102A can be modelled by a combination of a log-normal and Cauchy distribution. The break in our power-law fit occurs close to the energy threshold where these two functions in their fit merge ($\sim 10^{38}$ erg).

The two potential groups of bursts we have identified are unlikely to inhabit mutually exclusive areas of the parameter space. Instead, as can be seen from the energy distribution, the burst rate for high-fluence bursts from both groups is lower than that for low-fluence bursts from the group: with sufficient observation time and activity from FRB 20121102A, the LEBs and HEBs will partially overlap in their distributions. We compared the widths and fluences of our detected bursts with other bursts from FRB 20121102A at ~ 1.4 GHz that have been reported in the literature. In Figure 4 we plot the fluence against the width of our sample of bursts, as well as bursts from Rajwade et al. (2020), Oostrum et al. (2020), Cruces et al. (2021) and Li et al. (2021). The details of these other observations are summarised in Table 3. The forward-slanted V-shape seen in Figure 2 can also be seen here, although less distinctly, and the group of LEBs is broader and extends down to lower fluences due to the sensitivity of the FAST observations. We caution against over-interpreting the overlap of bursts in this figure, as widths and fluences are not always defined or calculated in a consistent manner. Oostrum et al. (2020) and Li et al. (2021) quoted boxcar widths and Rajwade et al., Cruces et al. (2021) and this work define the width as the FWHM of a Gaussian fit. Nevertheless, bursts from Rajwade et al. and Oostrum et al. inhabit the same parameter space as the HEBs, but their observations lacked the sensitivity to probe the LEB regime. Cruces et al. and Li et al. detected bursts that lie not only in the two groups our bursts inhabit, but also *in between* our LEBs and HEBs. We observed a total of ~ 59 hours, ~ 39 hours that fall within the proposed activity period

¹¹ https://docs.scipy.org/doc/scipy/reference/generated/scipy.optimize.curve_fit.html

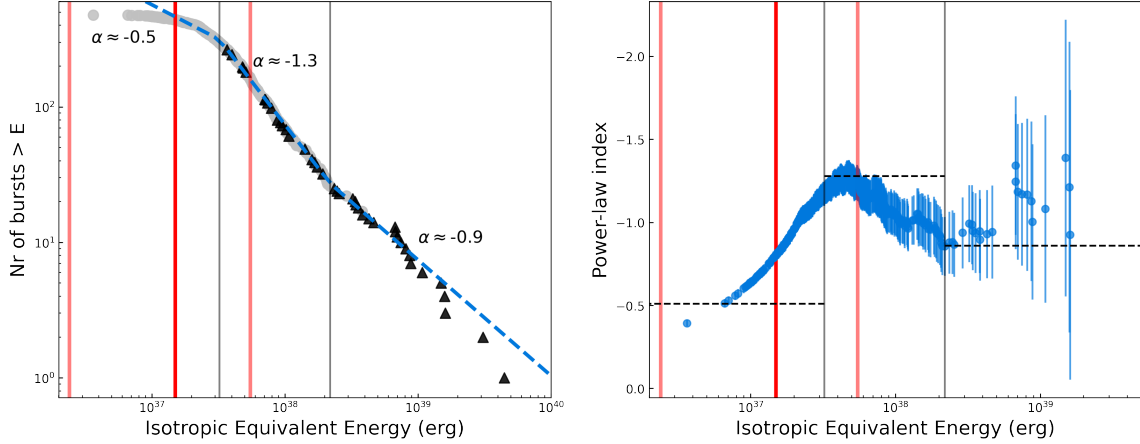


Figure 3. Left: The cumulative energy distribution and double broken power-law fit that excludes bursts below the sensitivity threshold (1.5×10^{37} erg). LEBs are indicated by grey circles and HEBs by black triangles. The vertical red line indicates this sensitivity threshold assuming a burst with a S/N of 6 and the mean burst properties of this sample, while the lighter red lines indicate best and worst case scenarios. The blue dashed line illustrates the broken power-law fit to the data, with the grey vertical lines indicating the breaks of the power-law fit. **Right:** the power-law index as a function of threshold energy calculated using a maximum-likelihood estimation. The horizontal dashed lines indicate the power-law indices obtained from fitting a broken power-law to the data with a least squares method. Vertical lines are the same as for the left panel.

of FRB 20121102A. In comparison, [Cruces et al.](#) observed ~ 128 hours, ~ 75 hours within the activity window and [Li et al.](#) observed ~ 60 hours all within the active period. Given that these authors spent more time observing during the active period than we did, this illustrates how with sufficient observation time rarer high-fluence LEBs (and HEBs) will be detected and the two groups will appear to merge in the fluence-width parameter space. It is also worth noting that the energy distribution of the bursts from FRB 20121102A has been seen to change over the course of one activity cycle ([Li et al. 2021](#)). Moreover, the burst activity from one cycle to the next has been shown to drastically change for FRB 20180916B. If the same mechanisms are at play in FRB 20121102A, this further complicates the comparison of observations during different activity windows.

In a comparison of burst fluences and luminosities, [Shannon et al. \(2018\)](#) found that FRBs detected by Parkes were on average of lower fluence, but higher DM than those detected by ASKAP. These different distributions arise from different telescope sensitivities and instantaneous field-of-view. Nonetheless, the Parkes and ASKAP FRBs have comparable luminosities (using DM as a proxy for distance). Additionally, the energies of bursts originally detected from FRB 20121102A were relatively low, compared to ASKAP and Parkes one-offs. This may lead one to speculate that the one-offs are in fact the most energetic bursts detected from repeaters. These FRBs are all plotted in an adapted version of the fluence-dispersion plot in Figure 5 ([Shannon et al. 2018; Petroff et al. 2019](#)). The properties of bursts from the two groups we identify in § 3.1 in fact correspond to some of the differences observed between one-off and repeating FRBs from the CHIME/FRB catalogue ([The CHIME/FRB Collaboration et al. 2021a](#)): HEBs and CHIME/FRB one-offs are typically broader band and shorter duration than LEBs and CHIME/FRB repeater bursts.

The analogy is, however, not perfect. [The CHIME/FRB Collaboration et al. \(2021a\)](#) have found no evidence to suggest that the fluence distributions of the bursts from the one-offs and repeaters are different. We have also overplotted both one-off, as well as repeating FRBs from the CHIME/FRB catalogue in Figure 5, and one can clearly see that these repeaters do not appear to be less luminous than the one-offs that have been detected. These fluence distributions are, however,

not fully representative of the underlying populations, as it can also be seen that the majority of current instruments lack the sensitivity to probe burst fluences below approximately 1 Jy ms. Should the known repeating FRBs be LEB equivalents and the observed one-offs be HEB equivalents, one would not necessarily expect them to have different fluence distributions. Rather, the burst fluence distributions of known repeaters would extend into the territory of one-offs. The brightest bursts from FRB 20121102A are comparable in luminosity to the one-offs detected by ASKAP and Parkes, and the faintest bursts extend beyond the sensitivity threshold of all but FAST (and, previously, that of Arecibo). Known repeaters exhibit a wide range of burst fluences and the nature and activity of low fluence bursts from FRBs remain a mystery for now.

Another potential caveat arises from the accumulating evidence in the literature that supports polarimetric differences between repeaters and one-offs. If all FRBs are repeaters and known repeaters are akin to LEBs while known one-offs are the HEBs, the polarimetric properties of LEBs and HEBs are expected to be different. We do not perform any polarimetric studies as the frequency resolution of our data is insufficient to resolve the high RM of FRB 20121102A at our observing frequency, but others have found no polarisation from any FRB 20121102A bursts at ~ 1.4 GHz ([Li et al. 2021](#)). Polarisation is, however, detected at ~ 4.5 GHz ([Michilli et al. 2018b](#)), so the lack of polarisation at ~ 1.4 GHz could potentially be due to the extreme local environment of the source imparting depolarisation at lower frequencies ([Plavin et al. submitted](#)).

Finally, we consider the argument presented in [Gourdji et al. \(2019\)](#) that fainter ‘smudge-like’ bursts are morphologically similar to higher energy multi-component bursts. [Gourdji et al. \(2019\)](#) presented a sample of 41 low-energy bursts from FRB 20121102A (almost all of which are also presented here) and showed that the narrowbandedness of fainter bursts might be explained by receiver sensitivity that is insufficient to detect fainter sub-components. This argument suggests that the LEBs are merely the ‘tips of the iceberg’, but HEBs possessing smaller temporal widths in general than LEBs contradicts this notion.

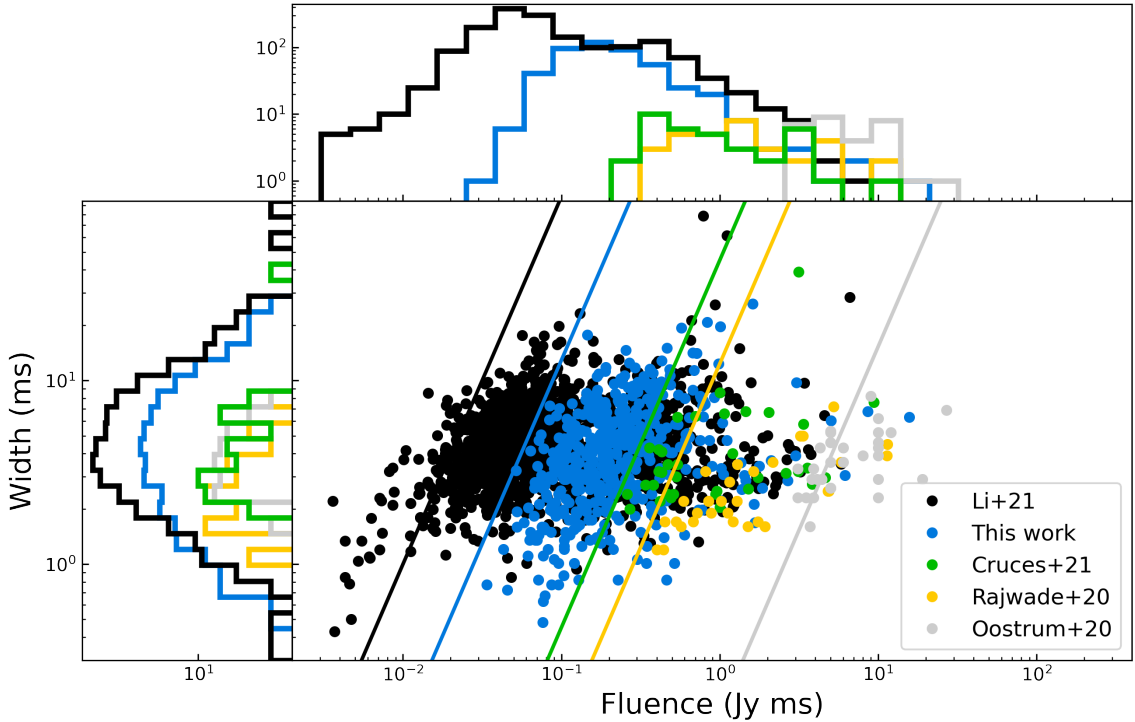


Figure 4. Width-fluence distribution for our Arecibo-detected bursts in blue, as well as for bursts from FAST (Li et al. 2021), Effelsberg (Cruces et al. 2021), Lovell (Rajwade et al. 2020) and Apertif (Oostrum et al. 2020) in black, green, yellow and grey, respectively. The diagonal lines represent the sensitivity threshold of the respective instruments. Side histograms in the left and top panel show the distribution of the burst width and fluence, respectively. These histograms also serve to indicate how clustered the data points in the main panel are. We caution against over-interpretation of the values being compared here, since the definition of ‘width’ and method of calculating the fluence are somewhat inconsistent between samples.

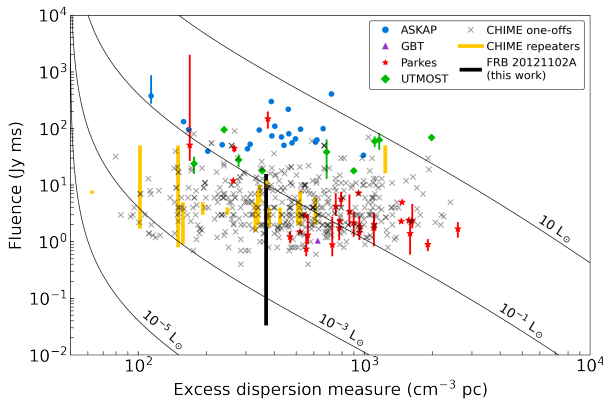


Figure 5. Fluence plotted against excess dispersion measure (corrected for the inferred Galactic foreground contribution) for the sample of bursts from FRB 20121102A detected in this paper (where the black vertical line indicates the range of fluences), as well as various other one-off and repeating FRBs. The different colours represent FRBs detected by different telescopes. Yellow bars indicate the range of fluences detected for CHIME/FRB repeaters. Lines of constant luminosity, assuming a DM contribution from the host galaxy $DM_{\text{host}} = 50 \text{ cm}^{-3} \text{ pc}$, are overplotted. Figure adapted from Shannon et al. (2018); Petroff et al. (2019).

4.2 Energy distribution

Studying the energy distribution of FRB 20121102A could reveal valuable information regarding the intrinsic emission mechanism of the bursts. As mentioned previously, there are many observational

biases that need to be accounted for and intricacies in energy calculations that make this a non-trivial task. We have already shown that the energy distribution of our bursts is reasonably well modeled by a double broken power-law, with breaks close to where LEBs and HEBs deviate from one another. Furthermore, the power-law index appears to be steepening from higher to lower energies, before decreasing again as the incompleteness regime is entered. We also observe that the power-law index is potentially changing from day to day, but lack the number of bursts required to concretely quantify this.

The energy distribution of bursts from FRB 20121102A has also been studied by various other authors (Law et al. 2017; Gourdji et al. 2019; Oostrum et al. 2020; Cruces et al. 2021; Aggarwal et al. 2021; Li et al. 2021). These authors have found different power-law slopes over different energy regimes (summarised in Table 3). Gourdji et al. (2019); Oostrum et al. (2020) and Cruces et al. (2021) made use of the maximum likelihood method we used in § 3.2, and calculate power-law indices of -1.8 ± 0.3 , -1.7 ± 0.6 and -1.1 ± 0.1 , respectively (albeit within different energy ranges). Aggarwal et al. (2021) estimate $-1.8 \pm 0.2 > E \approx 2 \times 10^{37} \text{ erg}$ by fitting a broken power-law. Law et al. (2017) find a less steep average power-law index of ~ -0.7 , irrespective of the burst frequencies (1.4 and 3.0 GHz bands) and burst rate, but notably refrain from estimating a completeness limit for their energy distributions, having a very small sample of bursts. Additionally, more observations over longer periods are also required to reveal how the time-dependent nature of the energy distribution as seen in Li et al. (2021) affects the slope of the energy distribution.

Magnetized neutron stars are promising candidates for compar-

ison of burst energy distributions, by reason of the multitude of theories which advocate for them as the progenitors of FRBs. There are a few pulsars, like the Crab pulsar (PSR B0531+21), that are known to display giant pulses (GPs; Heiles & Campbell 1970; Staelin 1970). GPs are typically very short (sometimes shorter than a ns) and 2 – 4 orders of magnitude brighter than normal pulses (e.g. Hankins et al. 2003; Hankins & Eilek 2007). The pulse-energy distribution of the GPs from the Crab pulsar obey a power-law (e.g. Argyle & Gower 1972; Lundgren et al. 1995; Popov & Stappers 2007; Karuppusamy et al. 2010), although the power-law index is typically much steeper ($-\alpha \approx 2 - 3$) than is observed for the energy distribution of FRB 20121102A. It is also worth noting that the V-shape seen in Figures 2 and 4 is similar to what is seen for GPs from the Crab pulsar, where the narrower GPs tend to be brighter (Karuppusamy et al. 2010; Popov & Stappers 2007). While the shape of the distribution is similar in width-energy parameter space, the timescales are much shorter for the Crab pulsar.

PSR J0540–6919 is another young pulsar that displays GPs. MeerKAT observations of this pulsar have yielded hundreds of GPs whose flux distribution can be fit a power-law with a very steep slope of -2.75 . Interestingly, there are also deviations from the power-law slope that are seen at all observing epochs (Geyer et al. 2021). These kinks are similar to the deviations we observe in our power-law fit. Only a small fraction of the GPs (< 3 per cent) were band-limited (only detected in a fraction of the band), implying that these kinks are not the result of narrow-bandedness.

4.3 Burst diversity and the average burst spectrum

Already at the time of its discovery as the first known repeating FRB, Spitler et al. (2016) remarked on the high variability between burst spectra. Many others have also noted the diversity in both the time and frequency properties of the bursts. That being said, the burst morphology of some of the more complex bursts is remarkably similar: e.g., the precursor bursts observed by Caleb et al. (2020) or the similarity between bursts AO-02 and GB-01 in Hessels et al. (2019). Whether this is a physically meaningful observation or mere coincidence remains to be seen. This diversity in the time and frequency properties of the bursts is showcased in Figure 1. The narrowest and widest bursts we detected are 0.5 (B205) and 26.0 ms (B107), respectively. The bursts also extend over different frequency ranges, with some being very narrowband (as narrow as ~ 65 MHz), while others extend over the whole observing bandwidth of 580 MHz. We found no evidence for periodic variation in any of the burst properties (see Appendix Figures A2–A5). We do, however, observe that the bursts from the same epoch are, on average, more similar to each other than to bursts from other epochs. This effect is especially difficult to quantify, due to the irregular burst rate. In Figure 6 the observed bandwidth of bursts are plotted against temporal widths for days where more than 40 bursts were detected. One can see, e.g., that a larger fraction of the bursts from MJD 57614 have larger bandwidths and that the bursts are of shorter duration compared to MJD 57628. For MJD 57614 and MJD 57628 the median bandwidths and widths are 292 MHz and 1.95 ms and 223 MHz and 5.08 ms, respectively. This might suggest an emission region that is evolving over the course of days, but stable over a period of \sim hours. However, the statistical significance of these apparent similarities of burst properties within an observing epoch is difficult to quantify and requires confirmation.

Figure 7 shows two different methods for determining the average spectrum of the bursts in our sample. In the middle panel the mean spectrum of the 435 LEBs and 43 HEBs detected from FRB 20121102A have been plotted as black and grey histograms,

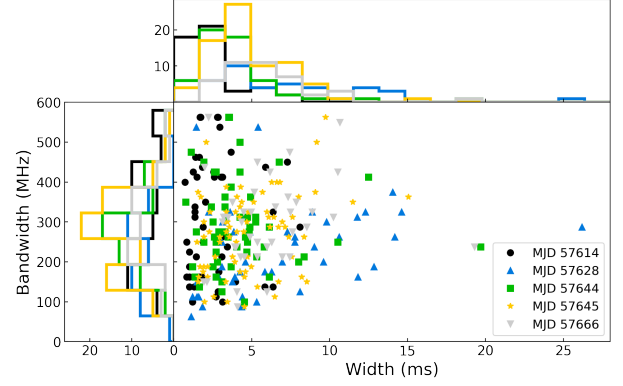


Figure 6. Bandwidth-width distribution of bursts from our sample on days where more than 40 bursts were detected. Different days are indicated by different colours (see the MJD in the legend). Side histograms in the left and top panels show the observed bandwidth and width distributions, respectively.

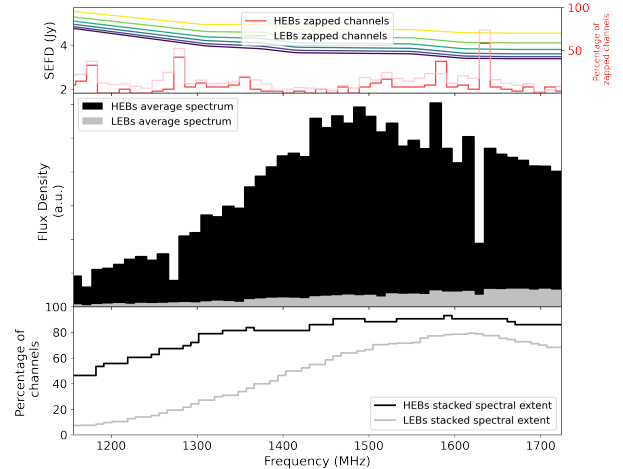


Figure 7. Top panel: The observational limitations. The red and pink histogram shows how many times each frequency channel was flagged due to the presence of RFI for the HEBs and LEBs, respectively. This is given as a percentage of the total number of bursts on the right hand y-axis. The SEFDs for zenith angles from 14 to 19 degrees, in steps of 1 degree, are shown on the left hand y-axis. **Middle panel:** The spectra obtained from averaging all the spectra for the HEBs (in black) and LEBs (in grey). **Bottom panel:** The percentage of bursts for which emission was present in a given channel for the HEBs in black and LEBs in grey.

respectively. These S/N-weighted average spectra are obtained by simply summing the spectra together of all the bursts in a group and then dividing by the number of bursts in that group. This plot shows that, on average, we observed factors of approximately 5 more burst emission at higher observing frequencies than at lower observing frequencies, for both the LEBs and HEBs. All spectra have been corrected for bandpass variations and the effect of decreasing sensitivity at lower frequencies has already been accounted for by modelling the SEFD of Arecibo as a function of frequency and zenith angle (see §3).

The top panel in Figure 7 shows the SEFD as a function of frequency for various zenith angles ranging from 14 degrees in dark blue to 19 degrees in yellow. Throughout the observation some channels were flagged more than once due the presence of RFI (manifesting as sharp dips in the average spectra in the middle panel). This decrease

in flux density that we observe at lower frequencies is thus not an effect of RFI excision.

The vast majority of bursts occur at the top of our observing band. We define the spectral extent of a burst as the 2-sigma region of a one-dimensional Gaussian fit to the time averaged spectrum of each burst. In the bottom panel of Figure 7 we stacked the spectral extents of all the bursts to produce an average ‘spectrum’ not weighted by signal intensity. This histogram thus indicates, given a burst detection, at which frequencies the burst emission is most likely visible. Here one can see that fewer bursts are detected at lower frequencies. For the LEBs, the shape is distinctly Gaussian-like and peaks at around 1600 MHz while dropping off quickly below 1400 MHz. Similarly, Gourdji et al. (2019) noted a “dearth” of bursts below 1350 MHz. The difference in the bandwidths between the LEBs and HEBs noted before is also apparent here. The HEBs are typically broader band. We found that the peak of the summed spectral extent remains more or less constant across our observations (see Appendix Figures A2–A5). We suspect that most, if not all, of the bursts detected at our highest observing frequencies extend beyond the observing band. The average stacked spectral extents presented here are thus not a representation of the average burst, but rather the frequency-dependent burst activity within our observing window.

Gajjar et al. (2018) plotted the peak flux density of a number of bursts in the literature as a function of frequency over a much larger frequency range of $\sim 1 - 8$ GHz, and found a relative flat spectral index with no evidence of a spectral turnover. Both Gajjar et al. (2018), as well as Zhang et al. (2018), do however find that the bursts they detected between 4 and 8 GHz seem to have preferred frequencies. This effect is, at least partly, due to Galactic scintillation. Nevertheless, our observations (made at lower frequencies than the previously mentioned authors), also support that the bursts from FRB 20121102A occur at preferential frequencies.

4.4 Activity window

In Figure 8 we illustrate the long-term monitoring at ~ 1.4 GHz with the Arecibo 305-m telescope of FRB 20121102A, since its discovery, as well as the activity cycles proposed by Rajwade et al. (2020) and Cruces et al. (2021). Rajwade et al. (2020) proposed a period of 157 days with a 56 per cent duty cycle, whereas the period from Cruces et al. (2021) is slightly different: 161 ± 5 days with a duty cycle of 54 per cent. After its discovery in 2012 (Spitler et al. 2014), FRB 20121102A was monitored again in 2013, and later in 2015 which resulted in the discovery of the first repeater burst detected from an FRB (Spitler et al. 2016). Long-term Arecibo monitoring commenced around December 2015, but ceased early in 2016. Observations again resumed towards the end of this first activity window of 2016, during which a few bursts were detected. The vast majority of the bursts presented in this paper come from the burst storm detected during the second active period in 2016. During this period and after confirmation of burst detections, we increased the frequency of our observations to approximately daily cadence starting from around \sim MJD 57640. The increased cadence, and consequently increased number of burst found, is evident in Figure 8. Now, aware of the activity window of FRB 20121102A, the lack of detections early in the project can easily be explained and supports the case for an activity window of ~ 161 days. We do, however, note that a subset of the bursts presented here (and also in Gourdji et al. (2019), Aggarwal et al. (2021) and Hessels et al. (2019)), were used together with other data to determine this activity window. Continued monitoring of FRB 20121102A in the coming years is necessary to refine this activity window and to determine its long-term stability or variability.

Any progenitor model for FRB 20121102A naturally needs to be able to explain this fairly long period activity window and large duty cycle. Xu et al. (2021) have shown that a supernova fallback disc with the most reasonable values for a disc wind can slow down isolated neutron stars to spin periods of hundreds of hours. A period similar to that of FRB 20121102A can be obtained by invoking an extremely large disc wind, but this challenges what may be physically possible around a magnetar. Wada et al. (2021) have shown that the large activity window of periodic FRBs can be explained by incorporating eccentricity in the binary comb model of Ioka & Zhang (2020). Furthermore, specifically for FRB 20121102A, and assuming the persistent radio source is in fact powered by a disc wind, a supermassive or intermediate-mass black hole companion is preferred over a massive star companion.

4.5 Wait times

Despite its long-term periodic activity, FRB 20121102A has shown no short-timescale periodicity in the arrival times of the bursts like that seen from pulsars or FRB 20191221A (The CHIME/FRB Collaboration et al. 2021b)¹², despite various searches using a range of techniques (Cruces et al. 2021; Aggarwal et al. 2021; Zhang et al. 2018). The wait times between bursts have been studied by other authors and form a bi-modal distribution with peaks at milli- and deca-seconds (Gourdji et al. 2019; Li et al. 2021; Aggarwal et al. 2021). We have calculated the wait times for our entire sample of bursts and also see two humps in the distribution. We fit the two humps with a log-normal function, by first excluding wait times < 1 s and then > 1 s. The wait time distribution and log-normal fits are presented in Figure 9. Additionally, we also calculated the wait times separately for the HEBs and LEBs. The HEBs show no sign of clustering in time (see also Appendix Figures A2–A5) and they typically have longer wait times, consistent with their lower rate. When taking into account all bursts, the log-normal functions peak at ~ 24 ms and ~ 95 s, which is comparable to what has been found by other authors (Zhang et al. 2018; Aggarwal et al. 2021). Aggarwal et al. (2021) have shown how the peak of the wait-times shifts to shorter timescales exponentially as more bursts are detected in a constant-length observation. The durations of our observations are tabulated in Table 1. The median observation duration is ~ 3800 s and implies that we are not sensitive to wait times longer than a few kiloseconds.

The peak at longer timescales is consistent with what is expected from a Poissonian distribution. The sub-second peak, in combination with the absence of wait times around one second, potentially describes the typical event duration. At least some fraction of the sub-second wait times are also likely the wait times between sub-bursts, where the faintest sub-bursts are not being detected. This ‘sub-burst’ peak is very evident in Li et al. (2021) at ~ 3 ms. In their wait time distribution a second sub-second peak can be seen (but is not explicitly mentioned) corresponding the one we observe. The sub-second peak we detect is also consistent with those found by Aggarwal et al. (2021) and Li et al. (2021), and support the claims made by the latter authors that challenge the feasibility of certain coherent emission models that require orderly magnetic field lines.

¹² This FRB is a single 3 s event with sub-second periodicity between sub-bursts.

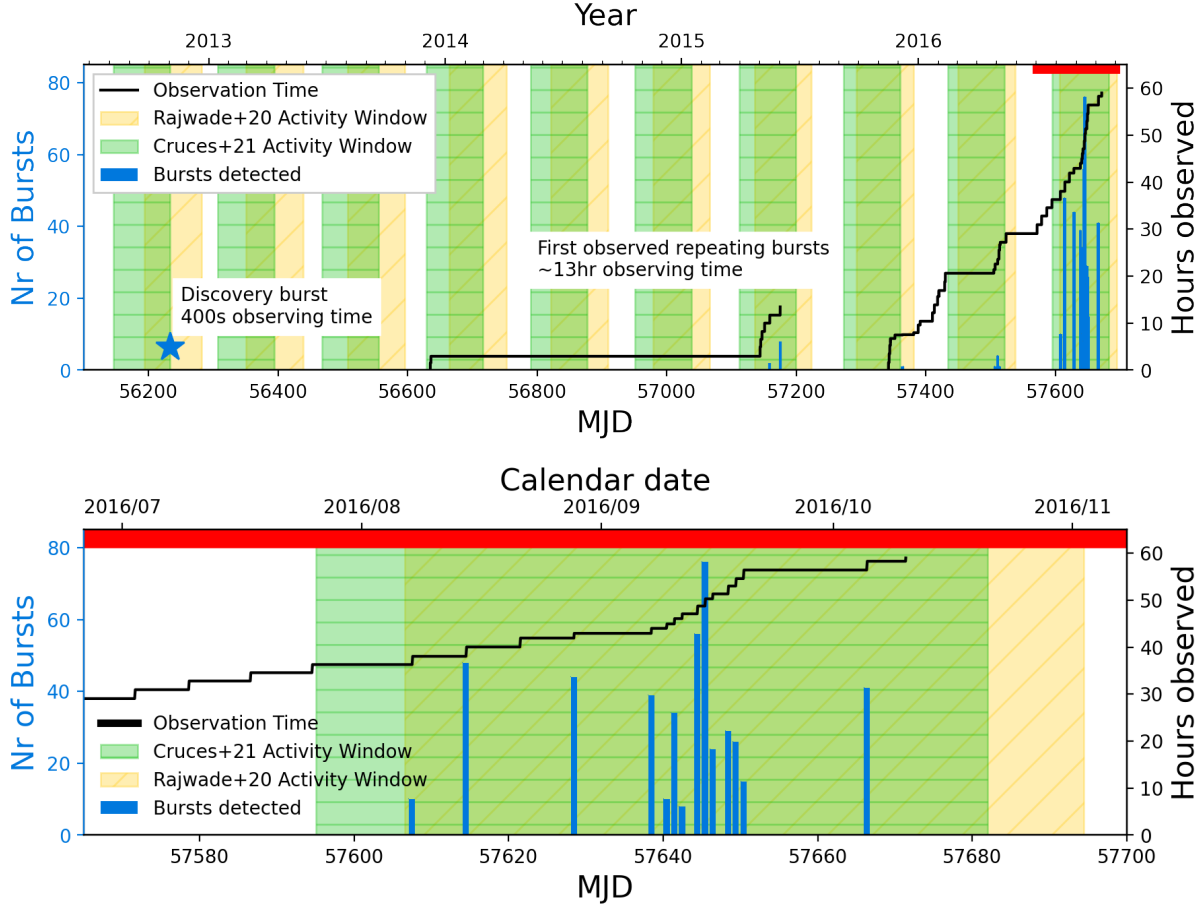


Figure 8. Timeline of Arecibo monitoring of FRB 20121102A, showing all the FRB 20121102A bursts detected with Arecibo at ~ 1.4 GHz up until the end of 2016. MJD is indicated on the bottom axes and calendar date on the top axes. The blue star indicates the date of the first burst ever to be detected from (Spitler et al. 2014). Blue histogram bars indicate the number of bursts detected in different observations (left axes). Note the first ten repeat bursts in mid-2015 that were presented in Spitler et al. (2016) and the first burst that was detected with PUPPI at the end of 2015 and presented in Scholz et al. (2016). The cumulative time spent observing is shown in black (right axes), and is reset to zero on MJD 57342, which is when the observations started that we report on in this paper. The tentative activity windows proposed by Rajwade et al. (2020) and Cruces et al. (2021) are shown as yellow and green shaded areas, respectively. The bottom panel is a zoom in of the top panel, at the dates indicated by the thick horizontal red bar. Bursts from MJD 57644 and MJD 57645 were also presented in Gourdji et al. (2019) and Aggarwal et al. (2021).

5 SUMMARY

In this paper we have reported on the detection of 478 bursts from FRB 20121102A that were obtained through monitoring with the Arecibo telescope at L-band, between December 2015 and October 2016. Our observations total ~ 59 hours, and reflect the earliest large observing campaign of this iconic source. Our analysis is summarised as follows.

- (i) The bursts in our sample are not all identical and divide into two groups in the width-bandwidth-energy parameter space that we refer to as LEBs (low-energy bursts) and HEBs (high-energy bursts).
- (ii) Statistical comparison tests concur that the temporal width, observed bandwidth and fluence distributions for the HEBs and LEBs cannot be drawn from the same parent population.
- (iii) The HEBs are typically narrower and more broadband than the LEBs, echoing the differences between one-off and repeating FRBs.
- (iv) We fit the energy distribution of our sample with a double broken power-law that has breaks at $E_{\text{b1}} = 3.1 \times 10^{37}$ and $E_{\text{b2}} =$

2.3×10^{38} , with power-law slopes of -0.5 where $E_{\text{iso}} \leq E_{\text{b1}}$, -1.3 where $E_{\text{b1}} < E_{\text{iso}} < E_{\text{b2}}$, and -0.9 where $E_{\text{iso}} \geq E_{\text{b2}}$.

(v) We observed that bursts from the same epoch tend to be more similar to each other than to bursts from other epochs, but note that this observation requires confirmation.

(vi) The majority of the bursts in our sample occur at the top of our observing band (~ 1730 MHz) and like previous authors we note a downturn in bursts detected below ~ 1350 MHz.

(vii) Our observations (including those with non-detections) support the case for a ~ 160 day activity period with a ~ 55 per cent duty cycle.

(viii) We find two lognormal peaks in the wait time distribution at ~ 24 ms and ~ 95 s, consistent with previous measurements and indicative of an event duration and Poissonian rate, respectively.

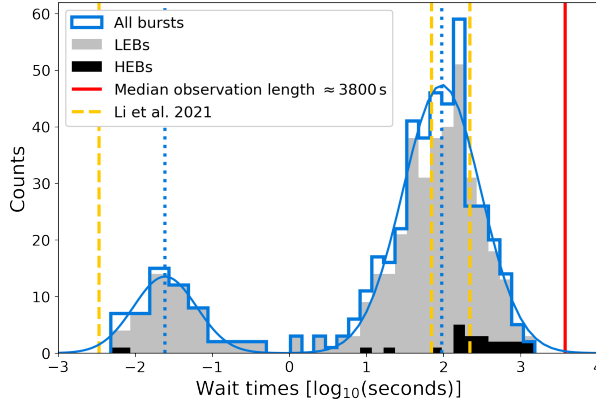


Figure 9. The wait time distribution for all detected bursts is shown by the blue outline. The separate wait time distributions for the LEBs and HEBs are indicated by solid grey and black histograms, respectively. Log-normal functions are fit to the full sample distribution above and below 1 second, and peak at ~ 24 ms and ~ 95 s as indicated by the dotted blue lines. Our sensitivity to longer wait times is degraded by the length of our observations. The median length of our observations is indicated by the red vertical line. For comparison, the peaks of the waiting times identified by Li et al. (2021) are indicated by yellow dashed vertical lines at 3.4 ± 1.0 ms, 70 ± 12 s and 220 ± 100 s. The latter being the peak for the higher energy bursts ($E > 3 \times 10^{38}$ erg) they observe.

ACKNOWLEDGEMENTS

Facility: Arecibo

Software: Astropy, FETCH, DSPSR, PSRCHIVE, PRESTO, psrfits_utils

Research by the AstroFlash group at University of Amsterdam, ASTRON and JIVE is supported in part by an NWO Vici grant (PI Hessels; VIDI.192.045). LGS is a Lise Meitner Max Planck Research Group Leader and acknowledges funding from the Max Planck Society.

DATA AVAILABILITY

The Arecibo data used in this work is available upon reasonable request.

REFERENCES

- Agarwal D., Aggarwal K., Burke-Spolaor S., Lorimer D. R., Garver-Daniels N., 2020, *MNRAS*, **497**, 1661
- Aggarwal K., 2021, *ApJ*, **920**, L18
- Aggarwal K., Agarwal D., Lewis E. F., Anna-Thomas R., Cardinal Tremblay J., Burke-Spolaor S., McLaughlin M. A., Lorimer D. R., 2021, arXiv e-prints, p. [arXiv:2107.05658](#)
- Argyle E., Gower J. F. R., 1972, *ApJ*, **175**, L89
- Bassa C. G., et al., 2017, *ApJ*, **843**, L8
- Beniamini P., Wadiasingh Z., Metzger B. D., 2020, *MNRAS*, **496**, 3390
- Bhandari S., et al., 2021, arXiv e-prints, p. [arXiv:2108.01282](#)
- Bochenek C. D., Ravi V., Belov K. V., Hallinan G., Kocz J., Kulkarni S. R., McKenna D. L., 2020, *Nature*, **587**, 59
- CHIME/FRB Collaboration et al., 2019a, *Nature*, **566**, 235
- CHIME/FRB Collaboration et al., 2019b, *ApJ*, **885**, L24
- CHIME/FRB Collaboration et al., 2020, *Nature*, **587**, 54
- Caleb M., et al., 2020, *MNRAS*, **496**, 4565
- Chatterjee S., et al., 2017, *Nature*, **541**, 58
- Chime/Frb Collaboration et al., 2020, *Nature*, **582**, 351
- Cordes J. M., Chatterjee S., 2019, *ARA&A*, **57**, 417
- Crawford D. F., Jauncey D. L., Murdoch H. S., 1970, *ApJ*, **162**, 405
- Cruces M., et al., 2021, *MNRAS*, **500**, 448
- Day C. K., et al., 2020, *MNRAS*, **497**, 3335
- Du S., Wang W., Wu X., Xu R., 2021, *MNRAS*, **500**, 4678
- Epps T., Singleton K., 1986, *Journal of Statistical Computation and Simulation*, **26**, 177
- Fonseca E., et al., 2020, *ApJ*, **891**, L6
- Gajjar V., et al., 2018, *ApJ*, **863**, 2
- Geyer M., et al., 2021, *MNRAS*, **505**, 4468
- Gourdji K., Michilli D., Spitler L. G., Hessels J. W. T., Seymour A., Cordes J. M., Chatterjee S., 2019, *ApJ*, **877**, L19
- Gu W.-M., Yi T., Liu T., 2020, *MNRAS*, **497**, 1543
- Hankins T. H., Eilek J. A., 2007, *ApJ*, **670**, 693
- Hankins T. H., Kern J. S., Weatherall J. C., Eilek J. A., 2003, *Nature*, **422**, 141
- Heiles C., Campbell D. B., 1970, *Nature*, **226**, 529
- Hessels J. W. T., et al., 2019, *ApJ*, **876**, L23
- Hilmarsson G. H., Spitler L. G., Main R. A., Li D. Z., 2021a, *MNRAS*, **508**, 5354
- Hilmarsson G. H., et al., 2021b, *ApJ*, **908**, L10
- Ioka K., Zhang B., 2020, *ApJ*, **893**, L26
- James C. W., Ekers R. D., Macquart J. P., Bannister K. W., Shannon R. M., 2019, *MNRAS*, **483**, 1342
- Josephy A., et al., 2019, *ApJ*, **882**, L18
- Karuppusamy R., Stappers B. W., van Straten W., 2010, *A&A*, **515**, A36
- Kirsten F., et al., 2021, arXiv e-prints, p. [arXiv:2105.11445](#)
- Kuerban A., Huang Y.-F., Geng J.-J., Li B., Xu F., Wang X., 2021, arXiv e-prints, p. [arXiv:2102.04264](#)
- Kumar P., Lu W., Bhattacharya M., 2017, *MNRAS*, **468**, 2726
- Kumar P., et al., 2019, *ApJ*, **887**, L30
- Kumar P., Shannon R. M., Lower M. E., Bhandari S., Deller A. T., Flynn C., Keane E. F., 2021, arXiv e-prints, p. [arXiv:2109.11535](#)
- Law C. J., et al., 2017, *ApJ*, **850**, 76
- Levin Y., Beloborodov A. M., Bransgrove A., 2020, *ApJ*, **895**, L30
- Li D., et al., 2021, *Nature*, **598**, 267
- Lorimer D. R., Bailes M., McLaughlin M. A., Narkevic D. J., Crawford F., 2007, *Science*, **318**, 777
- Lundgren S. C., Cordes J. M., Ulmer M., Matz S. M., Lomatch S., Foster R. S., Hankins T., 1995, *ApJ*, **453**, 433
- Luo R., et al., 2020, *Nature*, **586**, 693
- Lyutikov M., 2020, *ApJ*, **889**, 135
- Lyutikov M., Barkov M. V., Giannios D., 2020, *ApJ*, **893**, L39
- Marcote B., et al., 2017, *ApJ*, **834**, L8
- Margalit B., Beniamini P., Sridhar N., Metzger B. D., 2020, *ApJ*, **899**, L27
- Metzger B. D., Margalit B., Sironi L., 2019, *MNRAS*, **485**, 4091
- Michilli D., et al., 2018a, *MNRAS*, **480**, 3457
- Michilli D., et al., 2018b, *Nature*, **553**, 182
- Nimmo K., et al., 2021a, arXiv e-prints, p. [arXiv:2105.11446](#)
- Nimmo K., et al., 2021b, *Nature Astronomy*, **5**, 594
- Oostrum L. C., et al., 2020, *A&A*, **635**, A61
- Oppermann N., Yu H.-R., Pen U.-L., 2018, *MNRAS*, **475**, 5109
- Pedregosa F., et al., 2011, *Journal of Machine Learning Research*, **12**, 2825
- Petroff E., et al., 2016, *Publ. Astron. Soc. Australia*, **33**, e045
- Petroff E., Hessels J. W. T., Lorimer D. R., 2019, *A&ARv*, **27**, 4
- Petroff E., Hessels J. W. T., Lorimer D. R., 2021, arXiv e-prints, p. [arXiv:2107.10113](#)
- Platts E., Weltman A., Walters A., Tendulkar S. P., Gordin J. E. B., Kandhai S., 2019, *Phys. Rep.*, **821**, 1
- Platts E., et al., 2021, *MNRAS*, **505**, 3041
- Pleunis Z., et al., 2021, arXiv e-prints, p. [arXiv:2106.04356](#)
- Popov M. V., Stappers B., 2007, *A&A*, **470**, 1003
- Rajwade K. M., et al., 2020, *MNRAS*, **495**, 3551
- Ransom S. M., 2001, PhD thesis, Harvard University
- Scholz P., et al., 2016, *ApJ*, **833**, 177
- Shannon R. M., et al., 2018, *Nature*, **562**, 386
- Sob'yanin D. N., 2020, *MNRAS*, **497**, 1001
- Spitler L. G., et al., 2014, *ApJ*, **790**, 101

- Spitler L. G., et al., 2016, *Nature*, **531**, 202
 Staelin D. H., 1970, *Nature*, **226**, 69
 Tendulkar S. P., et al., 2017, *ApJ*, **834**, L7
 The CHIME/FRB Collaboration et al., 2021a, arXiv e-prints, [p. arXiv:2106.04352](#)
 The CHIME/FRB Collaboration et al., 2021b, arXiv e-prints, [p. arXiv:2107.08463](#)
 Thornton D., et al., 2013, *Science*, **341**, 53
 Wada T., Ioka K., Zhang B., 2021, *ApJ*, **920**, 54
 Xu K., Li Q.-C., Yang Y.-P., Li X.-D., Dai Z.-G., Liu J., 2021, *ApJ*, **917**, 2
 Yang H., Zou Y.-C., 2020, *ApJ*, **893**, L31
 Zanazzi J. J., Lai D., 2020, *ApJ*, **892**, L15
 Zhang Y. G., Gajjar V., Foster G., Siemion A., Cordes J., Law C., Wang Y., 2018, *ApJ*, **866**, 149

APPENDIX A: SOME EXTRA MATERIAL

Table 1. Observation log

Start MJD	Duration (s)	Nr of Bursts	Burst Rate (hr ⁻¹)
57342.225104167	5753.93497088	0	0
57343.223344907	6747.69141760	0	0
57344.224456019	6421.40602368	0	0
57345.227222222	3000.12273664	0	0
57345.263599537	1300.27618304	0	0
57345.280393519	971.86217984	0	0
57352.220868056	2705.46239488	0	0
57364.196805556	245.39824128	1	14.7
57381.179918981	1534.42320384	0	0
57388.099490741	5858.84499968	0	0
57391.152835648	1200.83972096	0	0
57391.131307870	1700.15064064	0	0
57410.039421296	6485.26430208	0	0
57413.040474537	6058.02201088	0	0
57418.019942130	6362.41313792	0	0
57420.016736111	465.16142080	0	0
57420.023229167	524.24867840	0	0
57420.029490741	606.54878720	0	0
57420.036678241	605.94585600	0	0
57420.043888889	598.40921600	0	0
57420.050983796	603.23266560	0	0
57420.058148148	602.02680320	0	0
57420.065289352	619.21034240	0	0
57428.986134259	6774.83642880	0	0
57429.988379630	6487.53971200	0	0
57504.819814815	625.50704128	0	0
57504.833935185	2175.13459712	0	0
57506.804212963	4262.69212672	1	0.8
57510.801192130	3579.10446080	4	4.0
57511.836574074	292.83581952	0	0
57512.759571759	6709.37645056	0	0
57513.786701389	4125.24478464	1	0.87
57514.809259259	1945.54888192	0	0
57523.730046296	6659.50617600	0	0
57571.597083333	6831.01126656	0	0
57578.579027778	6661.33069824	0	0
57586.561643519	6351.77009152	0	0
57594.541250000	6232.87205888	0	0
57607.507083333	6326.22678016	10	5.7
57614.479687500	7179.49501440	48	24.1
57621.460729167	6818.54369792	0	0
57628.446423611	3615.29081856	44	43.8
57638.448877315	3831.49670400	39	36.6
57640.412835648	808.26335232	10	44.5
57640.435451389	307.43199744	1	11.7
57640.464143519	2277.30784256	10	15.8
57641.438032407	4059.86607104	34	30.1
57642.439664352	3683.71040256	8	7.8
57644.407719907	5967.09998592	56	33.8
57645.409861111	5545.33126144	76	49.3
57646.394166667	3751.52181248	24	23.0
57648.393437500	6036.43183104	29	17.3
57649.394710648	5672.74373120	26	16.5
57650.380810185	6595.34381056	15	8.2
57666.338912037	6723.06036736	41	22.0
57671.374085648	2501.72407808	0	0
Total	212386.096087045	478	

Table 2. The statistical test results from the comparison between LEB and HEB properties

	KS statistic	p-value	Bootstrapping p-value
Width	0.47	3.0×10^{-8}	8.5×10^{-8}
Bandwidth	0.56	3.8×10^{-12}	1.3×10^{-10}
Fluence	0.63	2.0×10^{-15}	1.0×10^{-13}
	AD statistic	p-value	Bootstrapping p-value
Width	22.9	< 0.001	< 0.001
Bandwidth	50.5	< 0.001	< 0.001
Fluence	54.2	< 0.001	< 0.001
	ES statistic	p-value	Bootstrapping p-value
Width	63.3	5.9×10^{-13}	3.8×10^{-10}
Bandwidth	86.8	6.1×10^{-18}	1.4×10^{-12}
Fluence	39.9	4.6×10^{-8}	1.7×10^{-6}

Table 3. Observation properties of FRB 20121102A bursts at L-band

Telescope	SEFD (Jy)	Observing Frequency Range (MHz)	Observing Time (hrs)	Energy range (erg)	Power-law index
Apertif ^a	700	1130 – 1760	~130	$\sim 7 \times 10^{38} – 6 \times 10^{39}$	-1.7 ± 0.6
Arecibo (This work)	3.5	1150 – 1730	~57	$\sim 4 \times 10^{36} – 8 \times 10^{39}$	See Table A2
Arecibo ^b	2.9	1150 – 1730	~3	$\sim 7 \times 10^{36} – 2 \times 10^{38}$	-1.8 ± 0.3
Effelsberg ^c	17	1210 – 1510	~128	$\sim 1 \times 10^{38} – 1 \times 10^{39}$	-1.1 ± 0.1
FAST ^d	1.25	1050 – 1450	~60	$\sim 4 \times 10^{36} – 8 \times 10^{39}$ $\sim 3 \times 10^{38} – 8 \times 10^{39}$	-0.61 ± 0.04 -1.37 ± 0.18
Lovell ^e	38	1400 – 1800	~198	-	-

^aOostrum et al. (2020) ^bGourdji et al. (2019) ^cCruces et al. (2021) ^dLi et al. (2021), in this case the power-law fit is to the isotropic equivalent energy distribution rather than the cumulative-rate energy distribution. ^eRajwade et al. (2020)

Table A1: Burst properties

Burst ID	TOA ^a	Width (ms)	Bandwidth (MHz)	f_{high} (MHz)	f_{low} (MHz)	Fluence ^b (Jy ms)	Energy ^b (erg)	Group
1	57364.204636306	0.68 ± 0.05	> 546	> 1730	1184	0.08	4.0×10^{37}	HEB
2	57506.802409024	4.7 ± 0.3	> 381	> 1730	1349	0.38	1.3×10^{38}	LEB
3	57510.807219384	2.27 ± 0.09	> 546	> 1730	1184	0.29	1.4×10^{38}	HEB
4	57510.819153558	2.2 ± 0.3	> 305	> 1730	1425	0.11	2.9×10^{37}	LEB
5	57510.826409121	3.4 ± 0.2	> 419	> 1730	1311	0.27	1.0×10^{38}	LEB
6	57510.838080436	2.0 ± 0.2	> 267	> 1730	1463	0.19	4.3×10^{37}	LEB
7	57513.786194552	6.9 ± 0.4	> 508	> 1730	1222	0.38	1.7×10^{38}	LEB
8	57607.531624205	2.7 ± 0.2	> 331	> 1730	1399	0.30	7.3×10^{37}	LEB
9	57607.532581875	1.1 ± 0.2	> 217	> 1730	1513	0.09	1.5×10^{37}	LEB
10	57607.532581931	0.8 ± 0.1	> 217	> 1730	1513	0.10	1.6×10^{37}	LEB
11	57607.534122385	0.9 ± 0.2	> 141	> 1730	1589	0.10	1.3×10^{37}	LEB
12	57607.536338605	2.1 ± 0.3	> 414	1564	< 1150	0.09	2.7×10^{37}	LEB
13	57607.536916760	1.6 ± 0.3	> 356	> 1730	1374	0.08	2.3×10^{37}	LEB
14	57607.538497172	0.6 ± 0.1	> 153	> 1730	1577	0.08	8.2×10^{36}	LEB
15	57607.538801058	1.3 ± 0.2	> 166	> 1730	1564	0.10	9.9×10^{36}	LEB
16	57607.556613398	0.8 ± 0.2	> 128	> 1730	1602	0.09	9.2×10^{36}	LEB
17	57607.561407995	1.4 ± 0.3	> 179	> 1730	1551	0.10	1.2×10^{37}	LEB
18	57614.480578851	6.0 ± 1.0	> 141	> 1730	1589	0.39	4.6×10^{37}	LEB
19	57614.481112991	3.7 ± 0.6	> 483	> 1730	1247	2.10	7.0×10^{38}	HEB
20	57614.484578746	5.9 ± 0.7	> 445	> 1730	1285	0.19	7.5×10^{37}	LEB
21	57614.485018194	0.8 ± 0.2	> 166	> 1730	1564	0.13	1.7×10^{37}	LEB
22	57614.487302891	2.7 ± 0.5	> 115	> 1730	1615	0.30	2.5×10^{37}	LEB
23	57614.492513891	1.0 ± 0.3	164	1589	1425	0.12	1.7×10^{37}	LEB
24	57614.493918268	6.0 ± 1.0	329	1703	1374	0.18	5.1×10^{37}	LEB
25	57614.494855658	1.2 ± 0.2	> 103	> 1730	1627	0.21	2.0×10^{37}	LEB
26	57614.495491159	3.4 ± 0.5	> 242	> 1730	1488	0.15	2.8×10^{37}	LEB
27	57614.498991769	3.1 ± 0.6	> 217	> 1730	1513	0.15	2.7×10^{37}	LEB
28	57614.500237581	1.69 ± 0.01	> 580	> 1730	< 1150	1.67	8.7×10^{38}	HEB
29	57614.502912090	2.8 ± 0.4	> 580	> 1730	< 1150	0.15	7.4×10^{37}	LEB
30	57614.502912006	1.88 ± 0.09	> 293	> 1730	1437	0.37	8.7×10^{37}	HEB
31	57614.502912891	3.1 ± 0.5	> 419	> 1730	1311	0.09	3.2×10^{37}	LEB
32	57614.504828569	1.4 ± 0.03	> 470	> 1730	1260	0.44	1.7×10^{38}	HEB
33	57614.506268583	7.0 ± 2.0	> 457	> 1730	1273	0.08	3.2×10^{37}	LEB
34	57614.506322494	1.4 ± 0.3	> 331	> 1730	1399	0.07	2.1×10^{37}	LEB
35	57614.506902197	3.1 ± 0.4	> 275	1425	< 1150	0.12	2.9×10^{37}	LEB
36	57614.506902116	2.9 ± 0.5	> 179	> 1730	1551	0.21	2.7×10^{37}	LEB
37	57614.507729126	1.7 ± 0.1	> 580	> 1730	< 1150	0.15	7.1×10^{37}	HEB
38	57614.507815317	0.7 ± 0.1	> 407	> 1730	1323	0.05	1.5×10^{37}	LEB
39	57614.507982518	1.4 ± 0.1	> 318	> 1730	1412	0.17	4.8×10^{37}	HEB
40	57614.508122787	1.6 ± 0.4	> 166	> 1730	1564	0.13	1.7×10^{37}	LEB
41	57614.508801202	3.1 ± 0.6	> 103	> 1730	1627	0.16	1.5×10^{37}	LEB
42	57614.509636188	1.3 ± 0.2	> 141	> 1730	1589	0.18	2.3×10^{37}	LEB
43	57614.510669046	1.4 ± 0.2	> 217	> 1730	1513	0.11	1.6×10^{37}	LEB
44	57614.512576013	1.01 ± 0.07	> 141	> 1730	1589	0.34	3.7×10^{37}	HEB
45	57614.512697033	1.83 ± 0.06	> 452	1602	< 1150	0.29	1.1×10^{38}	HEB
46	57614.513259158	2.9 ± 0.3	> 546	> 1730	1184	0.10	4.8×10^{37}	LEB
47	57614.516194088	4.0 ± 0.9	> 153	> 1730	1577	0.22	2.9×10^{37}	LEB
48	57614.516825584	3.3 ± 0.6	279	1653	1374	0.11	2.5×10^{37}	LEB
49	57614.520871905	1.9 ± 0.4	> 255	> 1730	1475	0.10	2.2×10^{37}	LEB
50	57614.521175592	1.25 ± 0.09	> 432	> 1730	1298	0.13	5.1×10^{37}	HEB
51	57614.523279548	2.8 ± 0.6	> 128	> 1730	1602	0.21	2.3×10^{37}	LEB
52	57614.524042924	1.5 ± 0.06	> 419	> 1730	1311	0.32	1.0×10^{38}	HEB
53	57614.528465097	1.01 ± 0.04	> 191	> 1730	1539	0.52	7.9×10^{37}	HEB
54	57614.529631798	2.0 ± 0.4	354	1665	1311	0.06	1.9×10^{37}	LEB
55	57614.531688571	6.4 ± 0.5	> 141	> 1730	1589	0.79	9.3×10^{37}	LEB
56	57614.532182204	1.0 ± 0.2	228	1551	1323	0.10	1.8×10^{37}	LEB
57	57614.532413646	3.0 ± 0.6	> 419	> 1730	1311	0.07	2.7×10^{37}	LEB
58	57614.534391394	8.0 ± 1.0	291	1551	1260	0.92	2.2×10^{38}	LEB
59	57614.535610903	1.8 ± 0.3	164	1513	1349	0.12	1.9×10^{37}	LEB
60	57614.542240204	1.4 ± 0.3	> 343	> 1730	1387	0.07	1.9×10^{37}	LEB
61	57614.547262042	1.64 ± 0.05	> 470	> 1730	1260	0.40	1.6×10^{38}	HEB
62	57614.548318874	0.8 ± 0.1	> 255	> 1730	1475	0.07	1.4×10^{37}	LEB
63	57614.555657467	2.6 ± 0.3	> 432	> 1730	1298	0.13	4.6×10^{37}	LEB
64	57614.555656603	2.6 ± 0.7	418	1678	1260	0.08	2.6×10^{37}	LEB

Table A1: Burst properties (continued)

Burst ID	TOA	Width (ms)	Bandwidth (MHz)	f_{high} (MHz)	f_{low} (MHz)	Fluence (Jy ms)	Energy (erg)	Group
65	57614.555918484	2.85 ± 0.03	> 580	> 1730	< 1150	1.46	6.7×10^{38}	HEB
66	57628.447670509	2.2 ± 0.3	> 331	> 1730	1399	0.13	3.8×10^{37}	LEB
67	57628.450212308	7.8 ± 0.4	> 275	1425	< 1150	0.79	1.9×10^{38}	LEB
68	57628.450513580	5.0 ± 1.0	> 204	> 1730	1526	0.11	1.8×10^{37}	LEB
69	57628.451681533	4.2 ± 0.3	> 179	> 1730	1551	0.61	8.0×10^{37}	LEB
70	57628.451681888	5.0 ± 1.0	> 280	> 1730	1450	0.24	3.8×10^{37}	LEB
71	57628.451814085	14.0 ± 0.9	380	1653	1273	0.71	1.6×10^{38}	LEB
72	57628.452190991	1.0 ± 2.0	> 115	> 1730	1615	0.11	1.0×10^{37}	LEB
73	57628.452453495	13.0 ± 2.0	> 199	1349	< 1150	0.43	6.6×10^{37}	LEB
74	57628.454155076	1.8 ± 0.3	> 90	> 1730	1640	0.22	1.8×10^{37}	LEB
75	57628.456039490	9.0 ± 1.0	> 242	> 1730	1488	0.42	8.0×10^{37}	LEB
76	57628.456285007	2.9 ± 0.4	> 166	> 1730	1564	0.25	3.6×10^{37}	LEB
77	57628.459150027	1.6 ± 0.4	> 115	> 1730	1615	0.12	1.2×10^{37}	LEB
78	57628.459388175	7.0 ± 2.0	203	1691	1488	0.29	2.8×10^{37}	LEB
79	57628.459388703	6.0 ± 2.0	177	1374	1197	0.16	2.5×10^{37}	LEB
80	57628.459645746	12.0 ± 2.0	317	1640	1323	0.29	5.5×10^{37}	LEB
81	57628.460256544	8.0 ± 1.0	253	1627	1374	0.23	5.1×10^{37}	LEB
82	57628.460398778	10.0 ± 1.0	304	1691	1387	0.30	8.2×10^{37}	LEB
83	57628.460468926	15.0 ± 2.0	> 338	1488	< 1150	0.26	7.0×10^{37}	LEB
84	57628.461368709	1.1 ± 0.4	> 65	> 1730	1665	0.08	3.6×10^{36}	LEB
85	57628.461368913	3.8 ± 0.8	> 153	> 1730	1577	0.18	2.2×10^{37}	LEB
86	57628.462603963	7.3 ± 0.4	278	1627	1349	0.78	2.0×10^{38}	LEB
87	57628.463248271	12.0 ± 5.0	> 166	> 1730	1564	0.19	2.7×10^{37}	LEB
88	57628.463248953	1.5 ± 0.7	> 153	> 1730	1577	0.09	1.1×10^{37}	LEB
89	57628.463249190	8.9 ± 0.5	> 331	> 1730	1399	0.68	1.8×10^{38}	LEB
90	57628.463982619	3.1 ± 0.6	> 255	> 1730	1475	0.19	2.5×10^{37}	LEB
91	57628.465837536	3.6 ± 0.8	329	1640	1311	0.10	2.3×10^{37}	LEB
92	57628.465985991	14.0 ± 1.0	> 267	> 1730	1463	0.68	1.4×10^{38}	LEB
93	57628.466287593	3.9 ± 0.6	> 166	> 1730	1564	0.35	4.6×10^{37}	LEB
94	57628.467112907	10.6 ± 0.9	266	1564	1298	0.49	1.2×10^{38}	LEB
95	57628.468856965	3.1 ± 0.7	304	1678	1374	0.11	3.1×10^{37}	LEB
96	57628.468900621	12.3 ± 0.5	> 331	> 1730	1399	0.98	2.9×10^{38}	LEB
97	57628.468901111	3.1 ± 0.5	190	1374	1184	0.14	2.5×10^{37}	LEB
98	57628.469047862	5.4 ± 0.5	> 546	> 1730	1184	0.19	8.6×10^{37}	LEB
99	57628.469396408	4.3 ± 0.6	> 90	> 1730	1640	0.41	3.4×10^{37}	LEB
100	57628.472406218	8.0 ± 1.0	> 128	> 1730	1602	0.39	4.2×10^{37}	LEB
101	57628.472723636	4.4 ± 0.4	> 115	> 1730	1615	0.62	5.8×10^{37}	LEB
102	57628.472755687	6.0 ± 1.0	> 179	> 1730	1551	0.17	2.7×10^{37}	LEB
103	57628.474231593	5.0 ± 1.0	> 103	> 1730	1627	0.30	2.8×10^{37}	LEB
104	57628.477259734	4.5 ± 0.6	> 318	> 1730	1412	0.23	4.4×10^{37}	LEB
105	57628.479666172	1.2 ± 0.4	114	1488	1374	0.08	7.8×10^{36}	LEB
106	57628.479666986	10.0 ± 2.0	202	1475	1273	0.21	3.8×10^{37}	LEB
107	57628.479667381	26.0 ± 1.0	292	1501	1209	1.61	3.8×10^{38}	LEB
108	57628.480504366	1.45 ± 0.02	> 546	> 1730	1184	0.60	2.5×10^{38}	HEB
109	57628.485452123	3.9 ± 0.7	279	1691	1412	0.18	4.5×10^{37}	LEB
110	57638.453569021	8.0 ± 1.0	> 97	1247	< 1150	0.35	2.9×10^{37}	LEB
111	57638.455647134	1.5 ± 0.2	> 166	> 1730	1564	0.18	2.8×10^{37}	LEB
112	57638.457865366	4.3 ± 0.7	> 115	> 1730	1615	0.56	5.3×10^{37}	LEB
113	57638.457865669	4.8 ± 0.8	304	1627	1323	0.11	3.0×10^{37}	LEB
114	57638.457865968	2.9 ± 0.5	367	1703	1336	0.11	3.5×10^{37}	LEB
115	57638.458342337	2.4 ± 0.4	> 280	> 1730	1450	0.17	4.3×10^{37}	LEB
116	57638.458683219	3.9 ± 0.8	> 242	> 1730	1488	0.19	3.6×10^{37}	LEB
117	57638.458872587	11.3 ± 0.7	> 280	> 1730	1450	0.69	1.6×10^{38}	LEB
118	57638.459389010	8.7 ± 0.9	279	1501	1222	0.42	1.0×10^{38}	LEB
119	57638.460835678	11.0 ± 2.0	240	1437	1197	0.17	3.5×10^{37}	LEB
120	57638.461242351	5.5 ± 0.8	190	1488	1298	0.42	7.5×10^{37}	LEB
121	57638.463325785	4.7 ± 0.2	> 267	> 1730	1463	0.75	1.7×10^{38}	LEB
122	57638.463817296	0.8 ± 0.2	> 267	> 1730	1463	0.23	4.9×10^{37}	HEB
123	57638.465982995	2.6 ± 0.02	> 533	> 1730	1197	1.85	8.1×10^{38}	HEB
124	57638.466597987	4.4 ± 0.7	342	1577	1235	0.35	1.1×10^{38}	LEB
125	57638.467571141	3.42 ± 0.05	> 580	> 1730	< 1150	1.77	8.8×10^{38}	HEB
126	57638.468485337	2.4 ± 0.4	> 394	> 1730	1336	0.30	9.5×10^{37}	HEB
127	57638.469405606	1.7 ± 0.4	> 255	> 1730	1475	0.11	2.1×10^{37}	LEB
128	57638.469847028	4.0 ± 0.8	> 255	> 1730	1475	0.20	3.6×10^{37}	LEB

Table A1: Burst properties (continued)

Burst ID	TOA	Width (ms)	Bandwidth (MHz)	f_{high} (MHz)	f_{low} (MHz)	Fluence (Jy ms)	Energy (erg)	Group
129	57638.471731358	5.3 ± 0.7	> 580	> 1730	< 1150	0.13	6.3×10^{37}	LEB
130	57638.472320480	11.0 ± 2.0	> 305	> 1730	1425	0.19	4.9×10^{37}	LEB
131	57638.472988925	1.9 ± 0.4	> 217	> 1730	1513	0.17	3.0×10^{37}	LEB
132	57638.473566009	10.0 ± 2.0	241	1463	1222	0.24	5.2×10^{37}	LEB
133	57638.473943897	5.0 ± 2.0	> 280	> 1730	1450	0.17	4.3×10^{37}	LEB
134	57638.474845851	10.0 ± 1.0	> 432	> 1730	1298	0.35	1.3×10^{38}	LEB
135	57638.475544627	3.2 ± 0.3	304	1678	1374	0.26	7.0×10^{37}	LEB
136	57638.479543267	9.0 ± 1.0	> 267	> 1730	1463	0.39	8.7×10^{37}	LEB
137	57638.480763640	3.9 ± 0.6	> 331	> 1730	1399	0.15	4.2×10^{37}	LEB
138	57638.481443590	2.4 ± 0.4	> 369	> 1730	1361	0.21	5.0×10^{37}	LEB
139	57638.481457833	4.8 ± 0.8	> 229	> 1730	1501	0.30	5.8×10^{37}	LEB
140	57638.481457729	4.8 ± 0.8	> 115	> 1730	1615	0.18	1.7×10^{37}	LEB
141	57638.483365817	2.2 ± 0.4	> 77	> 1730	1653	0.18	1.3×10^{37}	LEB
142	57638.485971698	7.4 ± 0.9	> 495	> 1730	1235	0.24	9.5×10^{37}	LEB
143	57638.486501530	3.1 ± 0.7	> 407	> 1730	1323	0.11	3.9×10^{37}	LEB
144	57638.486502333	9.4 ± 0.9	> 318	> 1730	1412	0.42	1.2×10^{38}	LEB
145	57638.490459259	5.0 ± 1.0	> 217	> 1730	1513	0.26	4.3×10^{37}	LEB
146	57638.490931637	5.3 ± 0.7	304	1716	1412	0.32	8.1×10^{37}	LEB
147	57638.490932043	2.2 ± 0.4	215	1703	1488	0.13	2.2×10^{37}	LEB
148	57638.490931860	8.0 ± 0.9	> 103	> 1730	1627	0.60	5.7×10^{37}	LEB
149	57640.412997514	2.0 ± 0.3	> 280	> 1730	1450	0.13	3.2×10^{37}	LEB
150	57640.413845917	1.98 ± 0.03	> 580	> 1730	< 1150	0.73	3.6×10^{38}	HEB
151	57640.416032914	3.6 ± 0.4	> 369	> 1730	1361	0.20	6.4×10^{37}	LEB
152	57640.416790292	5.0 ± 1.0	240	1589	1349	0.12	2.6×10^{37}	LEB
153	57640.416894059	4.8 ± 0.7	> 445	> 1730	1285	0.15	6.1×10^{37}	LEB
154	57640.417060148	6.0 ± 1.0	> 419	> 1730	1311	0.15	5.6×10^{37}	LEB
155	57640.417568833	8.0 ± 1.0	> 90	> 1730	1640	0.28	2.3×10^{37}	LEB
156	57640.418180329	3.1 ± 0.5	> 432	> 1730	1298	0.11	4.0×10^{37}	LEB
157	57640.419506020	3.7 ± 0.8	> 204	> 1730	1526	0.16	2.4×10^{37}	LEB
158	57640.421280731	2.7 ± 0.4	> 153	> 1730	1577	0.17	2.2×10^{37}	LEB
159	57640.436390172	7.0 ± 2.0	> 331	> 1730	1399	0.16	5.0×10^{37}	LEB
160	57640.464985399	4.1 ± 0.6	> 242	> 1730	1488	0.18	4.1×10^{37}	LEB
161	57640.466011350	2.5 ± 0.5	> 356	> 1730	1374	0.10	3.3×10^{37}	LEB
162	57640.467145388	5.1 ± 0.5	456	1691	1235	0.18	7.3×10^{37}	LEB
163	57640.467269551	1.8 ± 0.3	> 445	> 1730	1285	0.09	3.7×10^{37}	LEB
164	57640.467269787	1.98 ± 0.05	> 508	> 1730	1222	0.43	1.9×10^{38}	HEB
165	57640.467905516	1.7 ± 0.3	> 204	> 1730	1526	0.16	2.6×10^{37}	LEB
166	57640.475221814	6.0 ± 1.0	> 179	> 1730	1551	0.27	3.5×10^{37}	LEB
167	57640.481356994	6.5 ± 0.8	279	1501	1222	0.31	8.0×10^{37}	LEB
168	57640.481356302	5.6 ± 0.9	342	1640	1298	0.24	7.8×10^{37}	LEB
169	57640.484934722	6.0 ± 1.0	> 166	> 1730	1564	0.30	4.2×10^{37}	LEB
170	57641.438346556	5.7 ± 0.7	> 267	> 1730	1463	0.25	5.9×10^{37}	LEB
171	57641.441395327	21.0 ± 1.0	> 318	> 1730	1412	0.83	2.1×10^{38}	LEB
172	57641.441629412	10.0 ± 2.0	> 115	> 1730	1615	0.43	4.1×10^{37}	LEB
173	57641.443197696	7.0 ± 1.0	> 280	> 1730	1450	0.37	8.3×10^{37}	LEB
174	57641.444802755	6.0 ± 1.0	> 110	1260	< 1150	0.38	3.2×10^{37}	LEB
175	57641.445077360	5.5 ± 0.4	> 293	> 1730	1437	0.46	1.2×10^{38}	LEB
176	57641.446497152	5.5 ± 0.8	> 255	> 1730	1475	0.34	7.3×10^{37}	LEB
177	57641.449121618	3.5 ± 0.9	> 293	> 1730	1437	0.10	2.5×10^{37}	LEB
178	57641.449121888	5.3 ± 0.9	> 457	> 1730	1273	0.13	4.7×10^{37}	LEB
179	57641.449121477	7.1 ± 0.9	> 457	> 1730	1273	0.15	5.6×10^{37}	LEB
180	57641.449122648	5.0 ± 0.9	> 432	> 1730	1298	0.13	4.5×10^{37}	LEB
181	57641.450565325	2.2 ± 0.4	> 191	> 1730	1539	0.16	2.5×10^{37}	LEB
182	57641.451054804	3.8 ± 0.4	> 356	> 1730	1374	0.26	7.7×10^{37}	LEB
183	57641.451174836	3.0 ± 0.5	> 242	> 1730	1488	0.14	2.6×10^{37}	LEB
184	57641.454929249	11.0 ± 2.0	> 217	> 1730	1513	0.38	6.3×10^{37}	LEB
185	57641.455221994	1.9 ± 0.5	190	1539	1349	0.09	1.5×10^{37}	LEB
186	57641.455326488	1.6 ± 0.3	342	1615	1273	0.05	1.6×10^{37}	LEB
187	57641.456844902	5.0 ± 1.0	368	1653	1285	0.13	3.8×10^{37}	LEB
188	57641.458226463	4.7 ± 0.7	> 280	> 1730	1450	0.29	6.9×10^{37}	LEB
189	57641.458887388	5.3 ± 0.8	304	1716	1412	0.20	5.3×10^{37}	LEB
190	57641.459208207	8.0 ± 2.0	> 343	> 1730	1387	0.14	4.2×10^{37}	LEB
191	57641.459464734	1.98 ± 0.03	> 580	> 1730	< 1150	0.77	3.8×10^{38}	HEB
192	57641.461578441	4.0 ± 1.0	> 318	> 1730	1412	0.10	2.8×10^{37}	LEB

Table A1: Burst properties (continued)

Burst ID	TOA	Width (ms)	Bandwidth (MHz)	f_{high} (MHz)	f_{low} (MHz)	Fluence (Jy ms)	Energy (erg)	Group
193	57641.464574073	6.32 ± 0.02	> 580	> 1730	< 1150	15.66	7.8×10^{39}	HEB
194	57641.464701394	4.9 ± 0.9	228	1653	1425	0.15	2.9×10^{37}	LEB
195	57641.466725543	1.2 ± 0.4	> 153	> 1730	1577	0.10	1.1×10^{37}	LEB
196	57641.468394863	5.2 ± 0.8	266	1627	1361	0.20	3.8×10^{37}	LEB
197	57641.471177469	5.0 ± 2.0	> 179	> 1730	1551	0.18	2.6×10^{37}	LEB
198	57641.471376428	6.0 ± 0.8	> 275	1425	< 1150	0.27	5.8×10^{37}	LEB
199	57641.476074500	4.1 ± 0.3	> 229	> 1730	1501	0.50	8.3×10^{37}	LEB
200	57641.477717141	3.9 ± 0.4	355	1539	1184	0.19	6.0×10^{37}	LEB
201	57641.481561999	6.5 ± 0.9	> 255	> 1730	1475	0.34	6.5×10^{37}	LEB
202	57641.482802698	2.5 ± 0.4	> 166	> 1730	1564	0.22	2.9×10^{37}	LEB
203	57641.483327074	2.4 ± 0.2	> 293	> 1730	1437	0.37	8.4×10^{37}	LEB
204	57642.454478620	6.0 ± 1.0	> 166	> 1730	1564	0.26	3.3×10^{37}	LEB
205	57642.454628075	0.5 ± 0.1	> 153	> 1730	1577	0.08	9.9×10^{36}	LEB
206	57642.455112897	3.1 ± 0.2	> 166	> 1730	1564	0.73	8.6×10^{37}	LEB
207	57642.469577903	3.3 ± 0.1	> 128	> 1730	1602	0.61	6.5×10^{37}	LEB
208	57642.469577973	3.3 ± 0.1	> 369	> 1730	1361	1.02	3.4×10^{38}	HEB
209	57642.471574283	3.91 ± 0.05	> 580	> 1730	< 1150	3.00	1.5×10^{39}	HEB
210	57642.475399913	2.8 ± 0.4	> 331	> 1730	1399	0.12	3.2×10^{37}	LEB
211	57642.475475746	3.04 ± 0.01	> 580	> 1730	< 1150	6.19	3.1×10^{39}	HEB
212	57644.408914198	2.4 ± 0.6	> 343	> 1730	1387	0.08	2.4×10^{37}	LEB
213	57644.409679758	2.6 ± 0.4	> 432	> 1730	1298	0.07	2.3×10^{37}	LEB
214	57644.409679901	2.7 ± 0.4	253	1627	1374	0.08	1.6×10^{37}	LEB
215	57644.410081666	2.6 ± 0.4	> 267	> 1730	1463	0.16	3.5×10^{37}	LEB
216	57644.411079675	3.6 ± 0.1	> 580	> 1730	< 1150	1.36	6.8×10^{38}	HEB
217	57644.411828715	1.1 ± 0.2	> 490	1640	< 1150	0.06	2.4×10^{37}	LEB
218	57644.412247927	4.2 ± 0.7	> 432	> 1730	1298	0.28	1.0×10^{38}	LEB
219	57644.412247700	2.7 ± 0.4	> 166	> 1730	1564	0.22	3.2×10^{37}	LEB
220	57644.414131227	11.0 ± 1.0	> 255	> 1730	1475	0.33	6.7×10^{37}	LEB
221	57644.414482490	3.7 ± 0.6	> 191	> 1730	1539	0.20	3.3×10^{37}	LEB
222	57644.414883361	3.3 ± 0.5	279	1640	1361	0.20	4.7×10^{37}	LEB
223	57644.414883124	3.3 ± 0.5	> 343	> 1730	1387	0.29	8.4×10^{37}	LEB
224	57644.416318802	4.7 ± 0.7	> 229	> 1730	1501	0.27	5.2×10^{37}	LEB
225	57644.418317841	3.0 ± 0.5	279	1716	1437	0.15	3.3×10^{37}	LEB
226	57644.418317922	2.5 ± 0.4	190	1678	1488	0.12	1.9×10^{37}	LEB
227	57644.420516004	2.8 ± 0.4	> 204	> 1730	1526	0.07	1.2×10^{37}	LEB
228	57644.423024306	2.9 ± 0.8	279	1564	1285	0.09	2.1×10^{37}	LEB
229	57644.423810235	3.3 ± 0.7	317	1602	1285	0.09	2.2×10^{37}	LEB
230	57644.428601393	5.0 ± 1.0	> 280	> 1730	1450	0.22	5.0×10^{37}	LEB
231	57644.430176669	1.6 ± 0.3	> 141	> 1730	1589	0.19	2.0×10^{37}	LEB
232	57644.430179357	4.6 ± 0.6	> 267	> 1730	1463	0.23	4.9×10^{37}	LEB
233	57644.430179900	3.5 ± 0.6	> 267	> 1730	1463	0.12	2.6×10^{37}	LEB
234	57644.431299561	2.0 ± 1.0	254	1653	1399	0.10	1.9×10^{37}	LEB
235	57644.432247887	1.4 ± 0.1	> 166	> 1730	1564	0.20	2.9×10^{37}	LEB
236	57644.434927012	2.9 ± 0.5	279	1691	1412	0.10	2.5×10^{37}	LEB
237	57644.436373736	12.0 ± 2.0	418	1665	1247	0.27	8.6×10^{37}	LEB
238	57644.436877379	6.0 ± 1.0	> 166	> 1730	1564	0.08	1.1×10^{37}	LEB
239	57644.438803711	5.3 ± 0.4	317	1678	1361	0.28	7.7×10^{37}	LEB
240	57644.438855871	6.8 ± 0.7	456	1665	1209	0.23	7.7×10^{37}	LEB
241	57644.439219632	4.2 ± 0.7	> 508	> 1730	1222	0.11	4.1×10^{37}	LEB
242	57644.440697286	2.5 ± 0.4	> 305	> 1730	1425	0.19	4.7×10^{37}	LEB
243	57644.443006600	8.3 ± 0.8	> 217	> 1730	1513	0.55	9.1×10^{37}	LEB
244	57644.443600774	1.9 ± 0.3	465	1615	< 1150	0.14	5.5×10^{37}	LEB
245	57644.445232447	3.7 ± 0.6	> 394	> 1730	1336	0.36	1.1×10^{38}	LEB
246	57644.446795897	0.8 ± 0.3	> 356	> 1730	1374	0.03	9.6×10^{36}	LEB
247	57644.447572196	4.2 ± 0.7	> 318	> 1730	1412	0.08	2.0×10^{37}	LEB
248	57644.447734501	4.7 ± 0.8	253	1488	1235	1.11	2.1×10^{38}	LEB
249	57644.448765577	2.7 ± 0.4	430	1627	1197	0.17	5.1×10^{37}	LEB
250	57644.448765269	3.3 ± 0.5	> 369	> 1730	1361	0.22	6.5×10^{37}	LEB
251	57644.449919919	5.0 ± 1.0	> 217	> 1730	1513	0.25	4.4×10^{37}	LEB
252	57644.451610530	4.9 ± 0.8	> 369	> 1730	1361	0.64	2.0×10^{38}	LEB
253	57644.452400502	4.7 ± 0.8	> 318	> 1730	1412	0.19	5.5×10^{37}	LEB
254	57644.452404524	4.5 ± 0.7	> 103	> 1730	1627	0.27	2.5×10^{37}	LEB
255	57644.453946248	2.7 ± 0.7	> 229	> 1730	1501	0.13	2.3×10^{37}	LEB
256	57644.454482060	8.0 ± 0.6	202	1475	1273	0.76	1.4×10^{38}	LEB

Table A1: Burst properties (continued)

Burst ID	TOA	Width (ms)	Bandwidth (MHz)	f_{high} (MHz)	f_{low} (MHz)	Fluence (Jy ms)	Energy (erg)	Group
257	57644.455958056	5.0 ± 1.0	304	1564	1260	0.14	3.6×10^{37}	LEB
258	57644.457891985	3.5 ± 0.5	> 580	> 1730	< 1150	0.10	4.9×10^{37}	LEB
259	57644.464763547	20.0 ± 2.0	> 242	> 1730	1488	1.01	1.9×10^{38}	LEB
260	57644.464764470	1.4 ± 0.4	> 280	> 1730	1450	0.07	1.5×10^{37}	LEB
261	57644.464764965	1.2 ± 0.6	190	1463	1273	0.04	6.6×10^{36}	LEB
262	57644.464767875	6.0 ± 1.0	291	1602	1311	0.17	4.2×10^{37}	LEB
263	57644.465671824	5.0 ± 2.0	> 293	> 1730	1437	0.10	2.3×10^{37}	LEB
264	57644.466232073	5.8 ± 0.5	> 242	> 1730	1488	0.52	9.3×10^{37}	LEB
265	57644.468106175	4.1 ± 0.6	> 242	> 1730	1488	0.49	9.8×10^{37}	LEB
266	57644.474725058	3.1 ± 0.5	> 153	> 1730	1577	0.20	2.3×10^{37}	LEB
267	57644.477086671	3.1 ± 0.5	> 128	> 1730	1602	0.47	5.0×10^{37}	LEB
268	57645.411095354	2.07 ± 0.07	> 508	> 1730	1222	0.37	1.7×10^{38}	HEB
269	57645.411657072	3.6 ± 0.5	266	1602	1336	0.24	5.6×10^{37}	LEB
270	57645.411897797	8.3 ± 0.9	266	1678	1412	0.44	1.0×10^{38}	LEB
271	57645.411897545	9.0 ± 3.0	152	1615	1463	0.17	2.4×10^{37}	LEB
272	57645.411925960	4.0 ± 1.0	393	1602	1209	0.10	3.3×10^{37}	LEB
273	57645.412288052	6.0 ± 1.0	> 318	> 1730	1412	0.18	4.8×10^{37}	LEB
274	57645.412287921	2.2 ± 0.7	> 166	> 1730	1564	0.09	1.2×10^{37}	LEB
275	57645.413651875	4.2 ± 0.6	> 343	> 1730	1387	0.19	6.1×10^{37}	LEB
276	57645.414466389	2.0 ± 1.0	> 103	> 1730	1627	0.09	7.1×10^{36}	LEB
277	57645.414466248	3.4 ± 0.7	> 331	> 1730	1399	0.10	2.9×10^{37}	LEB
278	57645.416103995	4.7 ± 0.7	> 313	1463	< 1150	0.16	4.0×10^{37}	LEB
279	57645.416405265	7.0 ± 1.0	> 407	> 1730	1323	0.17	5.3×10^{37}	LEB
280	57645.416569205	4.1 ± 0.8	> 280	> 1730	1450	0.16	3.7×10^{37}	LEB
281	57645.417474434	7.0 ± 1.0	405	1640	1235	0.17	5.9×10^{37}	LEB
282	57645.417906012	4.3 ± 0.6	> 356	> 1730	1374	0.17	5.3×10^{37}	LEB
283	57645.419013898	7.0 ± 1.0	> 305	> 1730	1425	0.15	3.8×10^{37}	LEB
284	57645.419217200	5.7 ± 0.9	380	1627	1247	0.12	3.5×10^{37}	LEB
285	57645.420273735	11.0 ± 2.0	355	1577	1222	0.48	1.5×10^{38}	LEB
286	57645.421293624	7.0 ± 1.0	> 293	> 1730	1437	0.19	4.8×10^{37}	LEB
287	57645.421299426	1.5 ± 0.3	380	1640	1260	0.08	2.4×10^{37}	LEB
288	57645.421618709	4.6 ± 0.9	177	1399	1222	0.20	3.1×10^{37}	LEB
289	57645.421853399	1.9 ± 0.4	> 186	1336	< 1150	0.12	1.6×10^{37}	LEB
290	57645.421883133	5.4 ± 0.7	> 141	> 1730	1589	0.44	5.2×10^{37}	LEB
291	57645.422462119	4.5 ± 0.6	> 280	> 1730	1450	0.24	6.3×10^{37}	LEB
292	57645.422576167	5.0 ± 1.0	> 166	> 1730	1564	0.11	1.6×10^{37}	LEB
293	57645.423020389	2.6 ± 0.5	> 115	> 1730	1615	0.15	1.4×10^{37}	LEB
294	57645.424155708	6.0 ± 1.0	> 331	> 1730	1399	0.12	3.1×10^{37}	LEB
295	57645.424628755	3.0 ± 1.0	> 305	> 1730	1425	0.07	1.8×10^{37}	LEB
296	57645.426801429	3.4 ± 0.8	278	1703	1425	0.12	3.1×10^{37}	LEB
297	57645.426931395	6.2 ± 0.9	> 293	> 1730	1437	0.19	4.8×10^{37}	LEB
298	57645.427343350	4.1 ± 0.9	> 369	> 1730	1361	0.09	2.9×10^{37}	LEB
299	57645.427343585	6.3 ± 0.8	405	1640	1235	0.16	5.6×10^{37}	LEB
300	57645.428914795	9.0 ± 1.0	> 508	> 1730	1222	0.26	1.2×10^{38}	LEB
301	57645.429909516	7.0 ± 2.0	152	1526	1374	0.16	2.1×10^{37}	LEB
302	57645.430354806	8.0 ± 2.0	317	1640	1323	0.19	4.9×10^{37}	LEB
303	57645.430453295	1.6 ± 0.5	> 166	> 1730	1564	0.08	1.0×10^{37}	LEB
304	57645.430632450	5.1 ± 0.6	> 356	> 1730	1374	0.23	6.7×10^{37}	LEB
305	57645.430632557	3.2 ± 0.5	> 305	> 1730	1425	0.19	4.7×10^{37}	LEB
306	57645.431311032	4.2 ± 0.8	> 179	> 1730	1551	0.18	2.8×10^{37}	LEB
307	57645.431482392	1.9 ± 0.2	> 191	> 1730	1539	0.19	3.4×10^{37}	LEB
308	57645.431879300	1.5 ± 0.4	> 255	> 1730	1475	0.06	1.2×10^{37}	LEB
309	57645.432302849	2.3 ± 0.6	> 331	> 1730	1399	0.08	2.3×10^{37}	LEB
310	57645.433097274	3.4 ± 0.7	> 394	> 1730	1336	0.09	3.1×10^{37}	LEB
311	57645.433642421	6.0 ± 2.0	> 318	> 1730	1412	0.09	2.4×10^{37}	LEB
312	57645.434336424	2.2 ± 0.4	> 191	> 1730	1539	0.20	3.1×10^{37}	LEB
313	57645.436213940	5.0 ± 1.0	330	1615	1285	0.10	3.1×10^{37}	LEB
314	57645.439100482	1.5 ± 0.4	> 153	> 1730	1577	0.12	1.6×10^{37}	LEB
315	57645.440821828	3.3 ± 0.3	> 153	> 1730	1577	0.42	5.5×10^{37}	LEB
316	57645.442108927	5.0 ± 0.9	> 191	> 1730	1539	0.20	3.4×10^{37}	LEB
317	57645.442638125	4.0 ± 0.7	254	1615	1361	0.15	3.1×10^{37}	LEB
318	57645.444485380	3.6 ± 0.4	> 293	> 1730	1437	0.16	4.3×10^{37}	LEB
319	57645.444928046	8.0 ± 0.9	367	1678	1311	0.25	8.1×10^{37}	LEB
320	57645.445449858	3.4 ± 0.7	> 103	> 1730	1627	0.18	1.7×10^{37}	LEB

Table A1: Burst properties (continued)

Burst ID	TOA	Width (ms)	Bandwidth (MHz)	f_{high} (MHz)	f_{low} (MHz)	Fluence (Jy ms)	Energy (erg)	Group
321	57645.448813374	1.7 ± 0.1	367	1678	1311	0.23	7.4×10^{37}	HEB
322	57645.449897206	4.0 ± 1.0	> 204	> 1730	1526	0.14	2.2×10^{37}	LEB
323	57645.449993809	2.7 ± 0.3	> 217	> 1730	1513	0.25	5.1×10^{37}	LEB
324	57645.449993490	15.0 ± 1.0	367	1640	1273	0.46	1.5×10^{38}	LEB
325	57645.451911113	8.0 ± 2.0	> 224	1374	< 1150	0.18	2.8×10^{37}	LEB
326	57645.451996554	4.7 ± 0.6	216	1577	1361	0.23	4.4×10^{37}	LEB
327	57645.451996431	1.7 ± 0.5	190	1539	1349	0.06	1.0×10^{37}	LEB
328	57645.453433171	2.9 ± 0.3	254	1577	1323	0.27	5.7×10^{37}	LEB
329	57645.453649376	8.2 ± 0.7	> 166	> 1730	1564	0.75	9.8×10^{37}	LEB
330	57645.453650545	7.0 ± 2.0	266	1716	1450	0.15	3.5×10^{37}	LEB
331	57645.454267497	6.0 ± 1.0	> 115	> 1730	1615	0.40	3.3×10^{37}	LEB
332	57645.454500380	4.2 ± 0.8	316	1627	1311	0.10	2.5×10^{37}	LEB
333	57645.458541565	1.9 ± 0.3	> 267	> 1730	1463	0.12	2.6×10^{37}	LEB
334	57645.459109533	3.8 ± 0.8	> 217	> 1730	1513	0.19	3.3×10^{37}	LEB
335	57645.46005809	10.0 ± 2.0	> 580	> 1730	< 1150	3.05	1.6×10^{39}	HEB
336	57645.462114524	7.1 ± 0.6	291	1551	1260	0.41	1.1×10^{38}	LEB
337	57645.464059788	4.0 ± 0.6	> 331	> 1730	1399	0.19	5.6×10^{37}	LEB
338	57645.464192686	4.8 ± 0.6	> 331	> 1730	1399	0.22	6.3×10^{37}	LEB
339	57645.464512080	3.0 ± 1.0	> 267	> 1730	1463	0.11	2.4×10^{37}	LEB
340	57645.465140151	1.9 ± 0.3	> 305	> 1730	1425	0.05	1.4×10^{37}	LEB
341	57645.466107341	2.3 ± 0.5	> 280	> 1730	1450	0.11	2.4×10^{37}	LEB
342	57645.466388384	4.5 ± 0.7	> 90	> 1730	1640	0.28	1.6×10^{37}	LEB
343	57645.474457941	9.0 ± 1.0	> 381	> 1730	1349	0.36	1.1×10^{38}	LEB
344	57646.396214077	4.0 ± 1.0	> 356	> 1730	1374	0.11	3.5×10^{37}	LEB
345	57646.396907193	3.0 ± 0.7	> 204	> 1730	1526	0.17	2.9×10^{37}	LEB
346	57646.398901505	5.0 ± 2.0	304	1703	1399	0.12	3.0×10^{37}	LEB
347	57646.400028116	7.0 ± 2.0	519	1716	1197	0.10	4.4×10^{37}	LEB
348	57646.400027668	2.9 ± 0.5	> 242	> 1730	1488	0.14	3.2×10^{37}	LEB
349	57646.403269343	8.0 ± 2.0	> 369	> 1730	1361	0.17	5.8×10^{37}	LEB
350	57646.403853712	8.0 ± 2.0	> 305	> 1730	1425	0.22	6.2×10^{37}	LEB
351	57646.404755675	6.0 ± 1.0	> 343	> 1730	1387	0.11	3.5×10^{37}	LEB
352	57646.412034945	8.0 ± 2.0	> 445	> 1730	1285	0.15	5.5×10^{37}	LEB
353	57646.416386908	4.4 ± 0.7	> 204	> 1730	1526	0.13	2.4×10^{37}	LEB
354	57646.417322886	3.42 ± 0.05	> 580	> 1730	< 1150	0.89	4.7×10^{38}	HEB
355	57646.418890723	6.8 ± 0.04	> 580	> 1730	< 1150	8.56	4.5×10^{39}	HEB
356	57646.420317180	3.1 ± 0.8	> 141	> 1730	1589	0.13	1.7×10^{37}	LEB
357	57646.425740788	3.4 ± 0.9	127	1716	1589	0.19	2.2×10^{37}	LEB
358	57646.426849863	4.2 ± 0.9	304	1640	1336	0.13	3.6×10^{37}	LEB
359	57646.427374892	3.7 ± 0.7	> 470	> 1730	1260	0.11	4.2×10^{37}	LEB
360	57646.427751317	2.7 ± 0.2	> 343	> 1730	1387	0.28	8.4×10^{37}	LEB
361	57646.427822616	6.0 ± 1.0	354	1665	1311	5.04	1.6×10^{39}	HEB
362	57646.428929651	2.1 ± 0.4	> 305	> 1730	1425	0.07	2.0×10^{37}	LEB
363	57646.432152691	4.7 ± 0.7	> 115	> 1730	1615	0.61	6.5×10^{37}	LEB
364	57646.432510181	10.0 ± 1.0	278	1475	1197	0.39	1.0×10^{38}	LEB
365	57646.433265786	1.8 ± 0.8	> 217	> 1730	1513	0.07	1.4×10^{37}	LEB
366	57646.435593599	5.0 ± 1.0	> 407	> 1730	1323	0.13	4.5×10^{37}	LEB
367	57646.437647438	18.0 ± 2.0	401	1551	< 1150	0.15	4.7×10^{37}	LEB
368	57648.394695267	4.8 ± 0.8	> 280	> 1730	1450	0.26	6.4×10^{37}	LEB
369	57648.394695722	5.1 ± 0.8	253	1716	1463	0.36	8.0×10^{37}	LEB
370	57648.397981691	6.0 ± 1.0	203	1526	1323	0.19	3.4×10^{37}	LEB
371	57648.398948127	3.0 ± 1.0	> 483	> 1730	1247	0.05	2.2×10^{37}	LEB
372	57648.398962032	9.0 ± 1.0	> 262	1412	< 1150	0.28	6.6×10^{37}	LEB
373	57648.398961675	6.1 ± 0.7	> 407	> 1730	1323	0.23	8.6×10^{37}	LEB
374	57648.400147951	5.1 ± 0.6	> 280	> 1730	1450	0.22	5.2×10^{37}	LEB
375	57648.405113326	2.9 ± 0.5	> 381	> 1730	1349	0.11	3.4×10^{37}	LEB
376	57648.407310973	2.6 ± 0.4	> 229	> 1730	1501	0.19	3.9×10^{37}	LEB
377	57648.408246646	3.6 ± 0.6	> 580	> 1730	< 1150	0.09	4.3×10^{37}	LEB
378	57648.408718285	7.0 ± 1.0	> 343	> 1730	1387	0.15	4.9×10^{37}	LEB
379	57648.409510113	6.0 ± 1.0	> 255	> 1730	1475	0.17	3.8×10^{37}	LEB
380	57648.416025020	3.9 ± 0.5	> 580	> 1730	< 1150	0.11	5.7×10^{37}	LEB
381	57648.416515289	3.3 ± 0.5	> 508	> 1730	1222	0.12	5.4×10^{37}	LEB
382	57648.418151268	2.6 ± 0.4	> 166	> 1730	1564	0.27	3.2×10^{37}	LEB
383	57648.420953720	3.6 ± 0.6	> 331	> 1730	1399	0.13	3.1×10^{37}	LEB
384	57648.425130860	2.8 ± 0.6	> 376	1526	< 1150	0.07	2.3×10^{37}	LEB

Table A1: Burst properties (continued)

Burst ID	TOA	Width (ms)	Bandwidth (MHz)	f_{high} (MHz)	f_{low} (MHz)	Fluence (Jy ms)	Energy (erg)	Group
385	57648.425557415	5.0 ± 1.0	> 580	> 1730	< 1150	0.07	3.8×10^{37}	LEB
386	57648.430800487	2.85 ± 0.04	> 445	> 1730	1285	2.68	1.1×10^{39}	HEB
387	57648.436824144	2.1 ± 0.1	> 445	> 1730	1285	0.14	5.2×10^{37}	LEB
388	57648.437795270	1.4 ± 0.6	> 580	> 1730	< 1150	0.06	3.0×10^{37}	LEB
389	57648.442284088	2.9 ± 0.5	> 255	> 1730	1475	0.11	2.3×10^{37}	LEB
390	57648.444075682	0.82 ± 0.03	> 224	1374	< 1150	0.46	9.3×10^{37}	HEB
391	57648.444075623	1.06 ± 0.07	> 262	1412	< 1150	0.30	7.1×10^{37}	HEB
392	57648.444238354	3.0 ± 0.5	> 229	> 1730	1501	0.21	4.2×10^{37}	LEB
393	57648.446202483	4.1 ± 0.7	304	1615	1311	0.06	1.7×10^{37}	LEB
394	57648.450881338	6.0 ± 1.0	228	1665	1437	0.19	3.8×10^{37}	LEB
395	57648.451852232	7.0 ± 1.0	228	1475	1247	0.31	5.9×10^{37}	LEB
396	57648.458118656	2.12 ± 0.08	> 293	> 1730	1437	1.64	4.3×10^{38}	HEB
397	57649.401228011	3.2 ± 0.5	114	1488	1374	0.11	1.0×10^{37}	LEB
398	57649.402088105	6.0 ± 1.0	228	1539	1311	0.32	3.0×10^{37}	LEB
399	57649.405568123	5.7 ± 0.7	> 267	> 1730	1463	0.54	3.2×10^{37}	LEB
400	57649.406038183	4.2 ± 0.6	317	1653	1336	0.45	4.3×10^{37}	LEB
401	57649.407710956	2.9 ± 0.5	431	1653	1222	0.20	2.3×10^{37}	LEB
402	57649.417338448	5.9 ± 0.3	266	1526	1260	1.04	1.1×10^{38}	LEB
403	57649.418685454	9.0 ± 1.0	> 186	1336	< 1150	0.34	3.6×10^{37}	LEB
404	57649.418874181	4.7 ± 0.4	> 229	> 1730	1501	0.86	4.1×10^{37}	LEB
405	57649.421654011	2.0 ± 0.5	> 331	> 1730	1399	0.09	9.4×10^{36}	LEB
406	57649.421654377	12.0 ± 2.0	> 186	1336	< 1150	0.36	3.9×10^{37}	LEB
407	57649.427776936	2.9 ± 0.5	> 580	> 1730	< 1150	0.42	9.8×10^{37}	LEB
408	57649.428169934	2.56 ± 0.03	> 580	> 1730	< 1150	1.37	3.4×10^{38}	HEB
409	57649.428772942	8.0 ± 2.0	> 580	> 1730	< 1150	0.17	3.7×10^{37}	LEB
410	57649.429578772	1.3 ± 0.2	> 90	> 1730	1640	0.35	1.6×10^{37}	LEB
411	57649.430031720	1.4 ± 0.2	> 293	> 1730	1437	0.17	1.2×10^{37}	LEB
412	57649.434472091	3.6 ± 0.3	> 439	1589	< 1150	0.30	6.0×10^{37}	LEB
413	57649.435394909	10.0 ± 2.0	342	1665	1323	0.49	4.6×10^{37}	LEB
414	57649.436190985	2.8 ± 0.7	114	1488	1374	0.15	1.5×10^{37}	LEB
415	57649.443162181	3.4 ± 0.3	> 224	1374	< 1150	0.24	2.5×10^{37}	LEB
416	57649.443315309	1.4 ± 0.3	215	1564	1349	0.15	1.4×10^{37}	LEB
417	57649.453910864	2.5 ± 0.7	> 204	> 1730	1526	0.26	1.2×10^{37}	LEB
418	57649.454126645	5.0 ± 1.0	> 255	> 1730	1475	0.61	2.9×10^{37}	LEB
419	57649.456815126	4.9 ± 0.7	> 267	> 1730	1463	0.42	2.5×10^{37}	LEB
420	57649.458481963	4.3 ± 0.8	317	1678	1361	0.31	2.9×10^{37}	LEB
421	57649.460566272	2.5 ± 0.6	> 191	> 1730	1539	0.28	1.3×10^{37}	LEB
422	57649.460566200	3.0 ± 1.0	> 318	> 1730	1412	0.08	8.9×10^{36}	LEB
423	57650.385611086	6.3 ± 0.7	> 356	> 1730	1374	0.28	9.0×10^{37}	LEB
424	57650.389382609	5.7 ± 0.8	> 217	> 1730	1513	0.21	4.2×10^{37}	LEB
425	57650.389383747	4.7 ± 0.8	> 414	1564	< 1150	0.07	2.6×10^{37}	LEB
426	57650.391440361	5.1 ± 0.9	> 293	> 1730	1437	0.21	5.8×10^{37}	LEB
427	57650.401579321	3.9 ± 0.6	241	1653	1412	0.12	2.7×10^{37}	LEB
428	57650.401745103	7.0 ± 2.0	> 381	> 1730	1349	0.13	4.2×10^{37}	LEB
429	57650.407361910	3.09 ± 0.05	> 351	1501	< 1150	1.05	3.2×10^{38}	HEB
430	57650.411402352	3.04 ± 0.02	> 580	> 1730	< 1150	1.43	7.5×10^{38}	HEB
431	57650.418154303	9.0 ± 1.0	> 267	> 1730	1463	0.30	7.5×10^{37}	LEB
432	57650.419939892	4.0 ± 0.6	> 229	> 1730	1501	0.19	4.1×10^{37}	LEB
433	57650.419990384	6.4 ± 0.9	253	1602	1349	0.25	5.6×10^{37}	LEB
434	57650.423670091	2.4 ± 0.8	> 255	> 1730	1475	0.10	2.3×10^{37}	LEB
435	57650.428279929	4.4 ± 0.7	> 166	> 1730	1564	0.25	3.3×10^{37}	LEB
436	57650.436131837	2.3 ± 0.2	> 166	> 1730	1564	0.33	5.0×10^{37}	LEB
437	57650.443053488	2.22 ± 0.04	> 267	> 1730	1463	1.02	2.5×10^{38}	HEB
438	57666.348165733	5.4 ± 0.6	> 255	> 1730	1475	0.28	5.7×10^{37}	LEB
439	57666.348938504	7.0 ± 2.0	367	1627	1260	0.19	6.1×10^{37}	LEB
440	57666.350467150	7.4 ± 0.5	> 217	> 1730	1513	0.81	1.4×10^{38}	LEB
441	57666.350914006	8.0 ± 2.0	355	1653	1298	0.14	4.3×10^{37}	LEB
442	57666.353529990	3.2 ± 0.5	317	1653	1336	0.16	4.0×10^{37}	LEB
443	57666.355441990	3.5 ± 0.8	> 318	> 1730	1412	0.09	2.7×10^{37}	LEB
444	57666.358917074	4.0 ± 1.0	> 217	> 1730	1513	0.13	2.4×10^{37}	LEB
445	57666.359189398	3.8 ± 0.8	> 356	> 1730	1374	0.12	3.5×10^{37}	LEB
446	57666.360757358	9.0 ± 2.0	> 331	> 1730	1399	0.17	4.4×10^{37}	LEB
447	57666.362653787	7.0 ± 1.0	> 224	1374	< 1150	0.25	4.8×10^{37}	LEB
448	57666.363801417	4.9 ± 0.7	> 267	> 1730	1463	0.24	5.4×10^{37}	LEB

Table A2. Power-law fit parameters

Single power-law	α_1				R^2	
All bursts	-0.87 ± 0.01				0.960887	
LEBs	-0.98 ± 0.01				0.943048	
HEBs	-0.46 ± 0.02				0.955989	
In-band bursts only	-0.72 ± 0.01				0.978148	
Broken power-law	α_1	E_{b1}	α_2		R^2	
All bursts	-0.503 ± 0.007	$3.22 \pm 0.02 \times 10^{37}$	-1.275 ± 0.009		0.996807	
LEBs	-0.568 ± 0.001	$3.27 \pm 0.02 \times 10^{37}$	-1.577 ± 0.02		0.994272	
HEBs	-0.339 ± 0.01	$2.9 \pm 0.2 \times 10^{38}$	-0.891 ± 0.05		0.993675	
In-band bursts only	-0.37 ± 0.01	$2.88 \pm 0.04 \times 10^{37}$	-0.906 ± 0.007		0.998105	
Double broken power-law	α_1	E_{b1}	α_2	E_{b2}	α_3	R^2
All bursts	-0.485 ± 0.008	$3.14 \pm 0.02 \times 10^{37}$	-1.258 ± 0.009	$2.3 \pm 0.8 \times 10^{38}$	-0.9 ± 0.2	0.996876
In-band bursts only	-0.42 ± 0.01	$3.16 \pm 0.04 \times 10^{37}$	-0.95 ± 0.01	$1.4 \pm 0.1 \times 10^{38}$	-0.68 ± 0.04	0.998335

Table A1: Burst properties (continued)

Burst ID	TOA	Width (ms)	Bandwidth (MHz)	f_{high} (MHz)	f_{low} (MHz)	Fluence (Jy ms)	Energy (erg)	Group
449	57666.367903239	5.0 ± 1.0	> 217	> 1730	1513	0.22	3.9×10^{37}	LEB
450	57666.369112460	4.3 ± 0.8	> 305	> 1730	1425	0.15	4.0×10^{37}	LEB
451	57666.369922217	3.1 ± 0.8	> 305	> 1730	1425	0.10	2.2×10^{37}	LEB
452	57666.375009891	6.3 ± 0.4	253	1589	1336	0.64	1.5×10^{38}	LEB
453	57666.376544430	6.0 ± 0.8	241	1539	1298	0.22	4.9×10^{37}	LEB
454	57666.376912287	2.22 ± 0.04	> 580	> 1730	< 1150	0.46	2.4×10^{38}	HEB
455	57666.377627586	4.1 ± 0.9	> 128	> 1730	1602	0.22	2.4×10^{37}	LEB
456	57666.379126956	9.0 ± 2.0	> 293	> 1730	1437	0.14	3.6×10^{37}	LEB
457	57666.379126664	7.0 ± 2.0	> 343	> 1730	1387	0.14	4.1×10^{37}	LEB
458	57666.382025231	6.0 ± 1.0	431	1691	1260	0.11	4.0×10^{37}	LEB
459	57666.383116333	7.0 ± 2.0	> 331	> 1730	1399	0.12	3.3×10^{37}	LEB
460	57666.384374390	4.1 ± 0.8	> 90	> 1730	1640	0.32	2.6×10^{37}	LEB
461	57666.388477979	11.0 ± 2.0	> 432	> 1730	1298	0.17	6.4×10^{37}	LEB
462	57666.389280667	4.0 ± 1.0	> 242	> 1730	1488	0.10	2.1×10^{37}	LEB
463	57666.389763841	5.0 ± 0.7	> 331	> 1730	1399	0.19	5.5×10^{37}	LEB
464	57666.389929171	10.0 ± 2.0	> 318	> 1730	1412	0.24	6.1×10^{37}	LEB
465	57666.394004959	5.4 ± 0.6	> 217	> 1730	1513	0.32	5.7×10^{37}	LEB
466	57666.400868763	7.0 ± 1.0	> 483	> 1730	1247	0.17	7.2×10^{37}	LEB
467	57666.400869314	19.0 ± 2.0	241	1615	1374	0.57	1.2×10^{38}	LEB
468	57666.401756404	5.4 ± 0.8	> 457	> 1730	1273	0.13	4.8×10^{37}	LEB
469	57666.403034982	5.2 ± 0.2	> 381	> 1730	1349	0.62	2.1×10^{38}	LEB
470	57666.403507575	4.0 ± 1.0	241	1412	1171	0.10	1.9×10^{37}	LEB
471	57666.403507772	1.9 ± 0.3	152	1399	1247	0.09	1.2×10^{37}	LEB
472	57666.404362343	11.0 ± 1.0	> 566	1716	< 1150	0.25	1.2×10^{38}	LEB
473	57666.405714957	8.0 ± 1.0	> 280	> 1730	1450	0.23	4.9×10^{37}	LEB
474	57666.405726895	2.0 ± 0.3	> 445	> 1730	1285	0.10	3.5×10^{37}	LEB
475	57666.407482295	5.2 ± 0.5	> 381	> 1730	1349	0.25	7.2×10^{37}	LEB
476	57666.411591271	2.1 ± 0.3	> 153	> 1730	1577	0.15	1.7×10^{37}	LEB
477	57666.412003453	4.5 ± 0.9	329	1640	1311	0.18	5.2×10^{37}	LEB
478	57666.417747468	6.0 ± 1.0	> 128	> 1730	1602	0.36	3.9×10^{37}	LEB

^a These times are dynamical times (TDB), corrected to the Solar System Barycenter to infinite frequency assuming a dispersion measure of 560.5 pc cm^{-3} and dispersion constant of $1/(2.41 \times 10^{-4}) \text{ MHz}^2 \text{ pc}^{-1} \text{ cm}^3 \text{ s}$. ^b We estimate a conservative 25 per cent uncertainty on these measurements due to uncertainty in the SEFD of Arecibo.

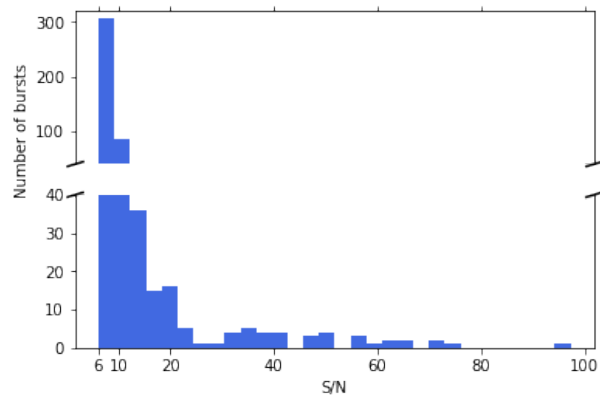


Figure A1. The S/N of all the bursts detected by PRESTO's `single_pulse_search.py`. This is the S/N of the boxcar with the highest S/N at the DM that maximises S/N.

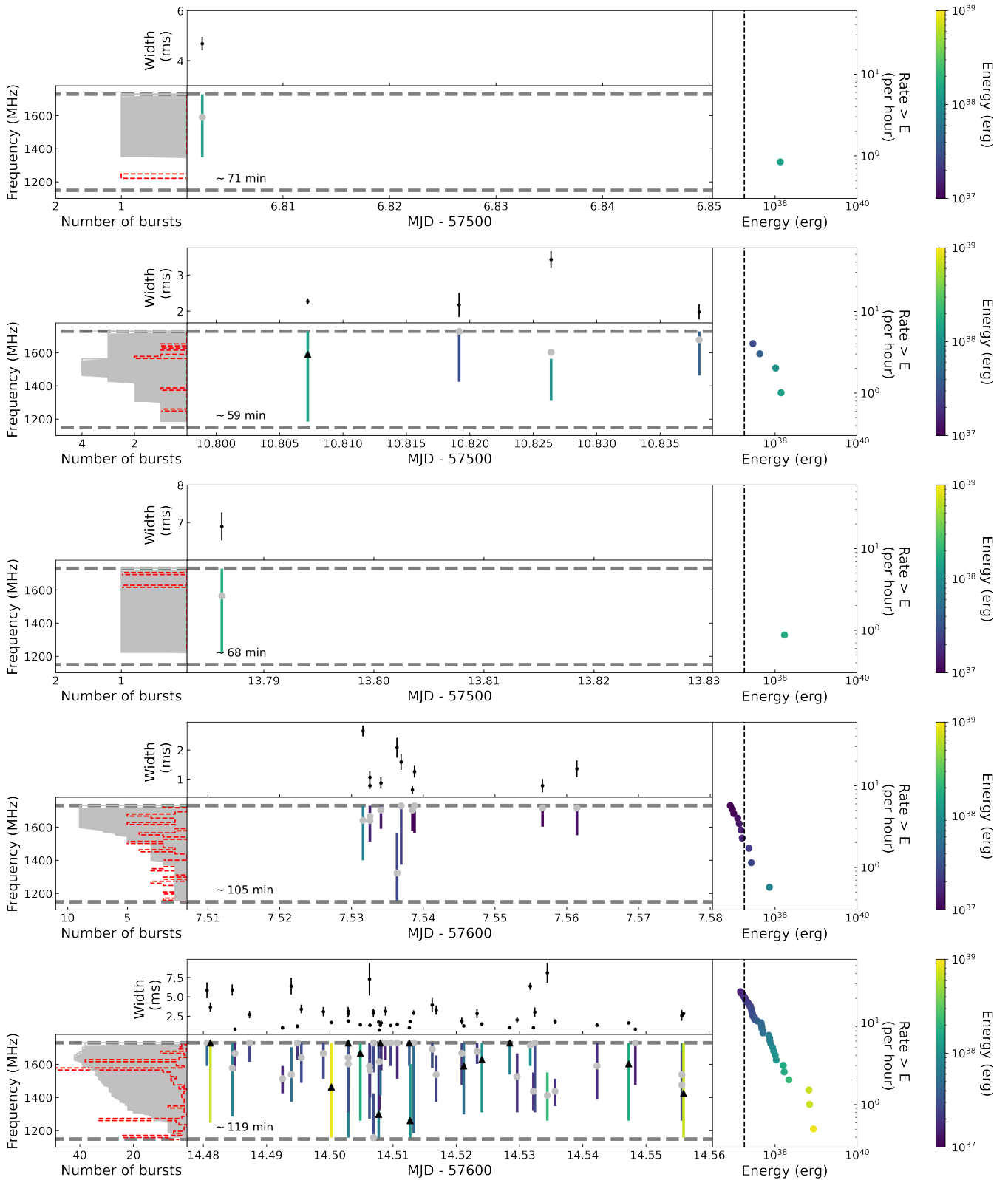


Figure A2. In Figures A2 – A5 the burst properties have been illustrated for all days on which bursts were detected. In the top panel the temporal width of the bursts is plotted as a function of the MJD. The range of the MJD x-axes are representative of the duration of each observation, and the scale changes between plots of different days. In the center bottom panel a vertical line, coloured according to the calculated isotropic equivalent energy of the burst, shows the spectral extent of each burst as a function of MJD. A grey circle or black triangle, indicates whether a burst is classified as a LEB or HEB, respectively, and is plotted on top of the line at the frequency corresponding to the peak of the Gaussian fit to the spectrum. All the vertical lines are stacked upon each other and displayed in the grey histogram in the left panel, illustrating the frequencies where a burst is most likely to be found during the observation. The overplotted red, dotted histogram indicates for how many bursts specific channels were flagged. Horizontal dashed grey lines at the top and bottom of the bottom panels represent the upper and lower edges of the observing band (1150 and 1730 MHz). Finally, in the right hand panel a burst energy cumulative distribution of the observation is shown, which has been colour-coded according to energies. These colours also correspond to the data points in the bottom center panel. Here we show MJDs 57506, 57510, 57513, 57607 and 57614. *MNRAS* **000**, 1–23 (2021)

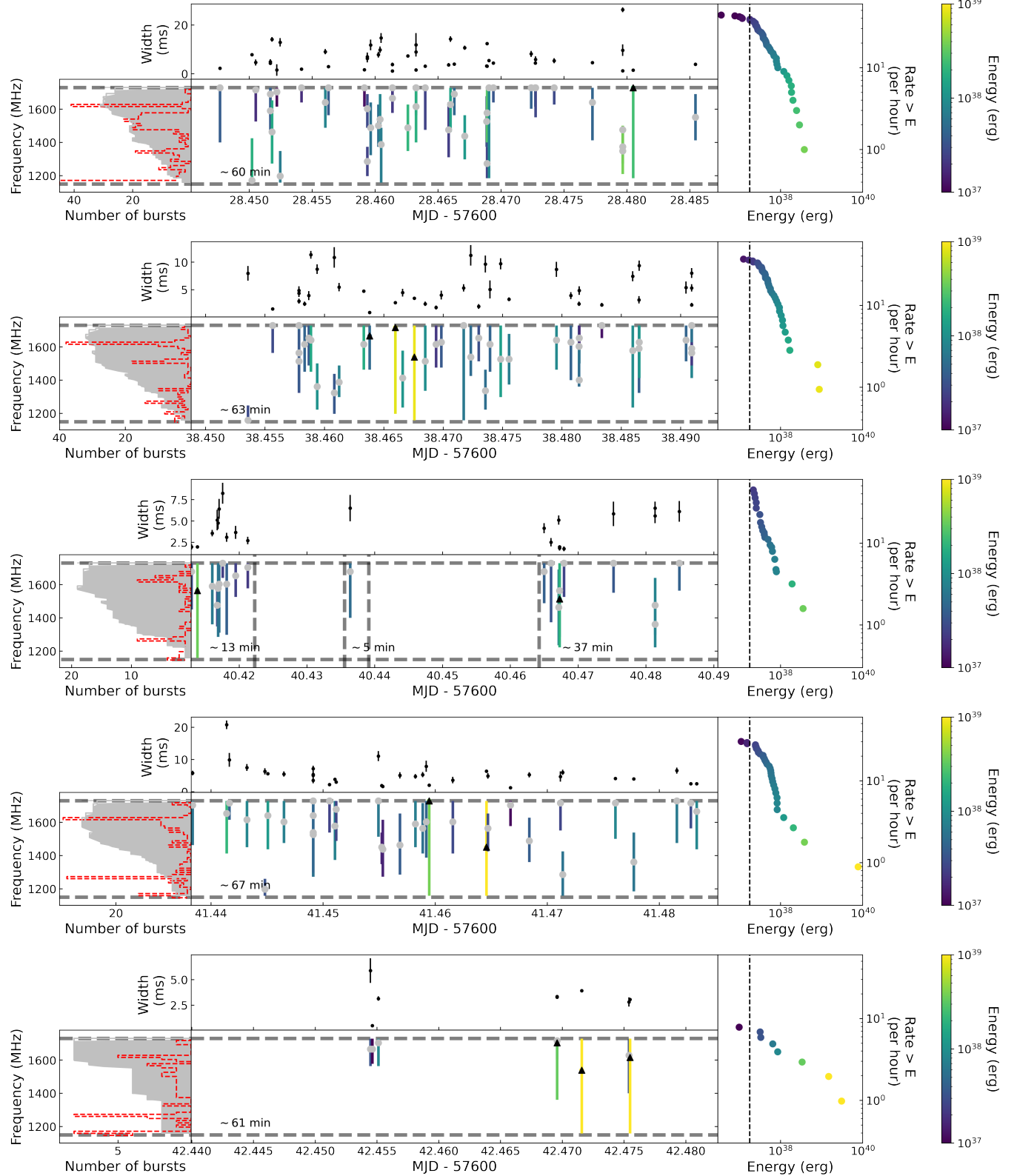


Figure A3. Same as A2, but for MJDs 57628, 57638, 57640, 57641 and 57642.

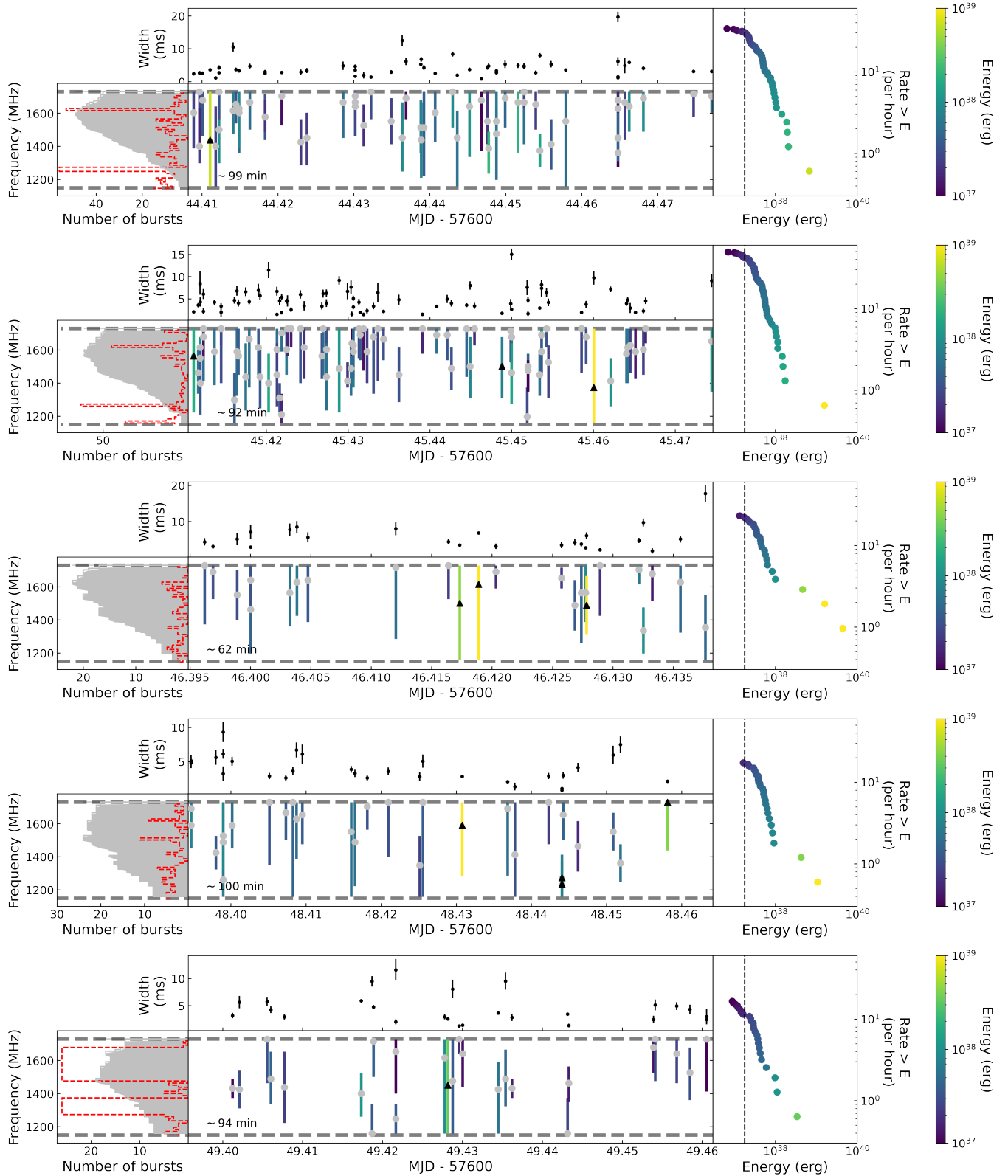


Figure A4. Same as A2, but for MJDs 57644, 57645, 57646, 57648 and 57649.

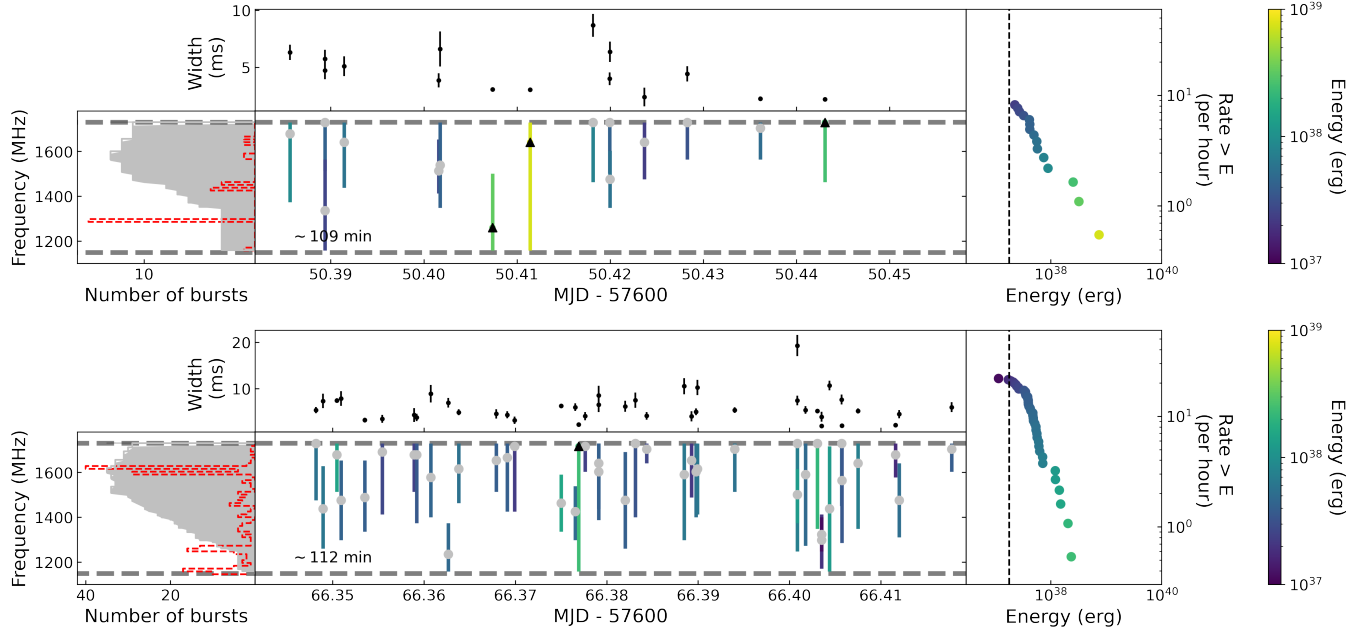


Figure A5. Same as A2, but for MJDs 57650 and 57666.